Geophysical and geochemical controls on abiotic carbon cycling on Earth-like planets

M. Neveu[1,2], T. Bartlow[1], R. Felton[3], S. Domagal-Goldman[2], S. Desch[4]

[1]University of Maryland, College Park, 4296 Stadium Drive, College Park, MD 20742, USA
[2]NASA Goddard Space Flight Center, 8800 Greenbelt Road, Greenbelt, MD 20771, USA
[3]NASA Ames Research Center, Moffett Field, CA 94043, USA
[4]Arizona State University, 781 E Terrace Mall, Tempe, AZ 85287

Key Points:

- A new code enables modeling of carbon cycling on planets of size and composition that differ from Earth's.
- Outgassing tends to go down with geologic time, is maximal for planets around 1 Earth mass, and higher for more felsic upper mantles.
- Continental weathering is comparatively less sensitive to surface composition and patchiness, and insensitive to planet size.

Corresponding author: Marc Neveu, `marc.f.neveu@nasa.gov`

Abstract

We investigate how variations in a planet's size and the chemical (mineral) composition of its upper mantle and surface affect processes involved in the carbonate-silicate cycle, which is thought to have regulated the composition of Earth's atmosphere and its surface temperature over geologic time. We present models of geophysical and geochemical controls on these processes: outgassing, continental weathering, and seafloor weathering, and analyze sensitivities to planet size and composition. For Earth-like compositions, outgassing is maximized for planets of Earth's size. Smaller planets convect less vigorously; higher pressures inside larger planets hinder melting. For more felsic mantles, smaller planets (0.5-0.75 Earth mass) outgas more, whereas more mafic planets follow the size trend of Earth's composition. Planet size and composition can affect outgassing by two orders of magnitude, with variability driven by mass in the first 2.5 Gyr after formation and by composition past that time. In contrast, simulations spanning the diversity of surface compositions encountered in the inner solar system indicate that continental weathering fluxes are about as sensitive to surface composition or the patchiness of land as they are to surface temperature, with fluxes within a factor of five of Earth's. Seafloor weathering appears more sensitive to uncertainties in tectonic regime (occurrence, speed, and size of plates) than to seafloor composition. These results form a basis to interpret calculations of geological surface carbon fluxes to track atmospheric compositions, through time, of lifeless exo-Earths, providing a baseline against which the effect of biological activity may be distinguished with telescopic observations.

Plain Language Summary

Earth's surface pressure and temperature have been relatively stable over its history. They are likely regulated by the greenhouse effect induced by carbon dioxide (CO_2) in Earth's atmosphere. CO_2 is thought to be outgassed from the mantle, e.g., through volcanism. CO_2 is removed from the atmosphere by chemical weathering (the reaction of surface rocks with CO_2-bearing rainwater), and river transport of its products to the ocean where carbonate rocks form. Carbonates are subducted to the mantle, completing the carbonate-silicate cycle. Here, we develop a model of mantle convection, melting, and chemical reactions between water and rock to investigate how this cycle might vary on solid planets with different sizes and mineral compositions. We find that these affect carbon outgassing more than weathering. This new ability to model carbon cy-

cling on a diversity of solid planets with an ocean helps understand what these planets might look like without a biosphere. Deviations from that baseline could be used to search for signs of life.

1 Introduction

Thousands of planets are now known to orbit stars other than our Sun (NASA Exoplanet Archive; Akeson et al. (2013)). Amidst the zoo of observed combinations of host-star types, star-planet distances, orbital eccentricities, and planet sizes, a handful of planets bearing similarities with Earth have been identified (Schulze-Makuch et al., 2011; Barnes et al., 2015; Kane et al., 2016; Gillon et al., 2017). These are primarily solid worlds for which "exo-climate" models have predicted temperatures that might allow surface liquid water (Wordsworth et al., 2011). Such potentially habitable worlds show promise as targets for detecting signs of life, e.g., via atmospheric spectral signatures (Krissansen-Totton et al., 2016; Grenfell, 2017; Schwieterman et al., 2018; Krissansen-Totton, Garland, et al., 2018; M. A. Thompson et al., 2022) in the coming decades (Kiang et al., 2018; Fujii et al., 2018; Pidhorodetska et al., 2020; Lin et al., 2021; Mikal-Evans, 2022).

Confidently attributing atmospheric spectral features to biology demands a thorough understanding of the physics, chemistry, and geology of exoplanets (Krissansen-Totton & Catling, 2017; Catling et al., 2018; Lisse et al., 2020). To detect life on an exoplanet, we must first constrain the geochemical cycles on a lifeless world, so that we recognize what is not attributable to abiotic processes. This requires the ability to model the interplay among interior, surface, atmospheric, and orbital processes, which is an overarching goal of the exoplanet community (Forget & Leconte, 2014; Lehmer et al., 2020; Barnes et al., 2020; Kopparapu et al., 2020; Unterborn et al., 2021; Krissansen-Totton et al., 2022).

Previous efforts to understand exoplanet geology and climate have so far focused on tidal (Barnes et al., 2013; Pierrehumbert & Hammond, 2019; Blackledge et al., 2020; Colose et al., 2021), orbital (Spiegel et al., 2009; Dressing et al., 2010; Kaspi & Showman, 2015; Lehmer et al., 2020; Vervoort et al., 2022), compositional (Bond et al., 2010; Young et al., 2014; Unterborn et al., 2014, 2016; Shahar et al., 2019; Unterborn et al., 2022), and land coverage controls (Abbot et al., 2012; Tziperman et al., 2012; Lewis et al., 2018; Krissansen-Totton, Arney, & Catling, 2018; Madden & Kaltenegger, 2020). Foley

(2015) has shown that the negative climate feedbacks inherent in the long-term carbon cycle are uninhibited by climate's effect on plate tectonics. Models of atmospheric chemistry and chemical evolution have assumed surface fluxes of gases from outgassing or weathering as lower boundary conditions (Hu et al., 2012; Domagal-Goldman et al., 2014; Felton et al., 2022), usually estimated from present Earth values (Edson et al., 2012; Krissansen-Totton & Catling, 2017; Krissansen-Totton, Arney, & Catling, 2018; Lehmer et al., 2020).

Outgassing rates have been predicted to increase with planet size (Kite et al., 2009). In addition, the oxidation state of a planet's environment influences the surface and atmospheric speciation of key elements such as carbon. Carbon is a chief component of planetary atmospheres as CO_2, CO, or CH_4; and an essential building block of life as we know it (Orgel, 1998). As CO_2, it is also a major control of Earth's climate via the carbonate-silicate cycle (Kasting, 1988). While some studies have probed the photochemistry of reduced carbon-rich atmospheres on terrestrial planets (Haqq-Misra et al., 2008; Arney et al., 2017; Felton et al., 2022), there is a need to investigate how the carbonate-silicate cycle might differ on worlds with a different bulk composition (Bond et al., 2010; Young et al., 2014; Unterborn et al., 2022).

To address this need, we have developed a model of geophysical and geochemical controls on abiotic cycling of carbon, on planets of 0.5 to 2 Earth masses ($M_\oplus$) with the same insolation as Earth. We use this model to investigate how the carbonate-silicate cycle varies depending on planet bulk composition, size, and age. The model incorporates key features of carbon cycling (Rushby et al., 2018): (1) equilibrium between atmospheric carbon and dissolved carbon in the ocean, (2) removal from the atmosphere by dissolving in rainwater and reacting with silicate rocks (weathering), (3) carbon removal from the ocean by seafloor water-rock interaction (Sleep & Zahnle, 2001; Krissansen-Totton & Catling, 2017), and (4) release of atmospheric carbon by outgassing such as volcanism or other venting. In this paper, we describe models for each of these processes that are validated to modern Earth conditions, but are based on first principles of geophysics and geochemistry rather than on scalings with modern-day Earth. This enables a departure from the necessarily Earth-centric conditions beyond which Earth-based scalings no longer accurately approximate the underlying outgassing and weathering processes. The present models can thus be used to investigate planets whose size and chemical composition differ from Earth's. In a companion paper, we describe the results of the integrated abiotic carbon cycling model.

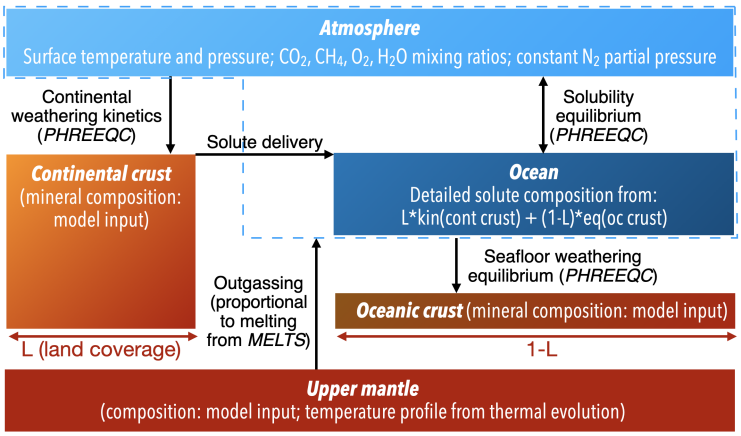

Figure 1. Architecture of the box model used to compute a planet's atmospheric and ocean composition as a function of time, with key computed parameters and inputs. The two reservoirs of carbon are the mantle and {atmosphere+ocean}. Fluxes between these reservoirs are due to seafloor weathering and mantle outgassing. The seafloor weathering flux depends on ocean composition, which itself depends on material fluxes arising from continental weathering and on ocean equilibrium with the atmosphere.

This paper is organized as follows. In Section 2, we describe the models of continental weathering, seafloor weathering, and outgassing, and their ability to reproduce corresponding estimated carbon fluxes on modern Earth. In Section 3, continental weathering and outgassing fluxes are computed for a variety of planet sizes and upper mantle or surface compositions. Sensitivity to these properties and their implications are discussed in Section 4; in particular, an example computation of the full carbon cycle through time is presented. We provide major conclusions in Section 5.

2 Model

The abiotic carbon cycling model (Fig. 1), determines net fluxes (in mol m^{-2} s^{-1}) of carbon species from the surface and interior to the atmosphere. We assume that these fluxes are primarily due to continental weathering, seafloor weathering, and outgassing, and that the atmosphere is equilibrated with the ocean into a single reservoir. This section focuses on describing models of each of these processes; description of their coupling in the overall model is provided in the companion paper. An implementation of the model in C language is freely available at https://github.com/MarcNeveu/ExoCcycleGeo.

2.1 Geodynamics and outgassing

Outgassing of a planet's interior to the atmosphere results from partial melting of mantle material advected to shallow depths (Kite et al., 2009). Although localized volcanism is a prominent form of outgassing, much of outgassing on a planet may occur from more diffuse (e.g., hydrothermal) sources. Both sources are linked to internal convection, melting, and subsequent conductive cooling of the crust. In this model, we do not distinguish subaerial from subaqueous outgassing because we consider the atmosphere and ocean as a single reservoir in which the atmosphere and ocean compositions are at equilibrium.

Our overall procedure for calculating outgassing fluxes is as follows. The thermal evolution of a planet of a given size is computed by balancing accretional and radiogenic heating with convective and conductive cooling (as a function of tectonic mode) to obtain temperature profiles as a function of depth at different time points in a planet's history. Geodynamic model parameters and adopted values are described in Table 1. These temperature profiles are used to determine the melt fraction as a function of depth for rock of a specified composition, using the *alphaMELTS* command line implementation (Smith & Asimow, 2005; R. N. Thompson et al., 2007; P. M. Antoshechkina & Asimow, 2010; P. M. Antoshechkina et al., 2010; P. Antoshechkina & Asimow, 2018) of the *MELTS* software (Ghiorso & Sack, 1995; Asimow & Ghiorso, 1998). From melt fractions, using the same simplifying assumption as Kite et al. (2009) that all melt reaches the surface (or at least the near-surface crust), we obtain rates of melt extrusion (or intrusion). Finally, we assume that the rate of carbon outgassing is directly proportional to that extrusion and intrusion rate, based on the assumed carbon content of the upper mantle material able to be outgassed.

2.1.1 Planet structure

The user inputs a planet mass, core mass fraction, and three materials for an inner core, outer core, and mantle. From these parameters, an interior structure is generated for the planet using the approach described in Lorenzo et al. (2014). The planet is divided in 1-dimensional grid zones, assuming spherical symmetry. Given a first-guess radius, the gravitational acceleration is computed as a function of depth. The equation of hydrostatic equilibrium is then integrated to find the pressure at depth, assuming con-

Table 1. Geodynamic model parameters. The lack of dependency for this study of the assumed values for the geodynamical parameters described in this section on a planet's bulk composition (Table 1) is addressed in Section 4. [a] User-specified inputs via planet mass, core mass fraction, and inner core, outer core, and mantle materials (Lorenzo et al., 2014).

Parameter	Symbol	Value	Units	Notes and references
Planet Structure				
Planet radius [a]	r_p		m	
Core-mantle boundary radius [a]	r_c		m	
Grid zone radius	r		m	
Gravitational acceleration	g		m s^{-2}	
Density [a]	ρ		kg m^{-3}	Lorenzo et al. (2014)
Pressure	P		Pa	$= \int_r^{r_p} \rho(r)\, g(r)\, dr$
Temperature	T		K	
Accretion				
Fraction of impactor energy deposited at depth	h	0.1		Canup et al. (2021)
Ratio of planetesimal velocity to escape velocity	χ	2.0		Canup et al. (2021)
Thermal Evolution				
Radiogenic power per unit mass	H		W kg^{-1}	Nuclide heating rate × mantle abundance (Table 2)
Radionuclide half-life	$t_{1/2}$		s	See Table 2
Mantle heat capacity	C_p	1295	J kg^{-1} K^{-1}	Akaogi and Ito (1993)
Mantle thermal conductivity	k	4.18	W m^{-1} K^{-1}	Turcotte and Schubert (2002)
Mantle thermal diffusivity	κ		m^2 s^{-1}	$= k/(\rho\, C_p)$
Mid-mantle temperature	T_m		K	From equation (4)
Surface temperature	T_s		K	
Mantle thermal expansivity	α	3×10^{-5}	K^{-1}	Turcotte and Schubert (2002)
Radius of brittle-ductile transition	r_{BDT}		m	
Temperature in mantle adiabat	T_{adiab}		K	From equation (5)
Temperature in lithosphere	T_{upbnd}		K	From equation (6)
Depth of lithosphere	z_{Lith}		m	Where $T_{adiab} = T_{upbnd}$
Rayleigh number	Ra		–	
Critical Rayleigh number	Ra_{cr}	1707.762	–	Reid and Harris (1958)
Nusselt number scaling parameter	β	1/3	–	$Nu = (Ra/Ra_{cr})^{\beta}$
Convective velocity	v_{conv}		m s^{-1}	From equation (7)
Convective timescale	t_{conv}		s	$= (r_{BDT} - r_c)/v_{conv}$

tinuity across core and mantle boundaries. Equations of state for each of the three materials are inverted to derive the densities as a function of pressure. Based on these densities, the thickness of the layers is adjusted. The gravitational acceleration as a function of depth is then updated, and so on until a convergence threshold is reached on the central density. Several equations of state are considered depending on the material: a third-order Birch-Murnaghan equation of state (Lorenzo et al., 2014), a power law (Seager et al., 2007), and for high-pressure phases of ice, a temperature-dependent equation (Choukroun & Grasset, 2010). A database of planetary materials and equation-of-state parameters is provided with the code and includes data from Seager et al. (2007) for α-(bcc)Fe, $MgSiO_3$, (Mg,Fe)SiO_3, high-pressure H_2O, C (graphite), and SiC; Dubrovinsky et al. (2000) for ϵ-Fe; W. W. Anderson and Ahrens (1994) for liquid Fe; Fei et al. (1995) for FeS IV; Sata et al. (2010) for FeS VII; Duffy, Hemley, and Mao (1995) for MgO; Weidner et al. (1982) for SiO_2; Wett and Ahrens (1983) for Mg_2SiO_4; Chung (1971) for $(Mg,Fe)_2SiO_4$; Duffy, Meade, et al. (1995) for $Mg(OH)_2$; Tyburczy et al. (1991) for serpentine; Nestola et al. (2010) for antigorite; Auzende et al. (2006) for lizardite; Fortes et al. (2013) for $Na_2SO_4{\cdot}10H_2O$; Gromnitskaya et al. (2013) for $MgSO_4{\cdot}7H_2O$; Choukroun and Grasset (2010) for liquid H_2O and its ices Ih, II, III, V, and VI; Frank et al. (2013) for H_2O ice VII; Fortes et al. (2003) for $NH_3{\cdot}2H_2O$ I; Griffiths et al. (2012) for $NH_3{\cdot}2H_2O$ IIa; and Ma et al. (2012) for $NH_3{\cdot}2H_2O$ liquid. A typical grid comprises 10^4 zones. This is much finer than required for this structure calculation, but necessary to resolve the upper mantle finely enough as to accurately compute melting as a function of depth. The oversampling of deeper layers seldom affects the speed of computation because the planetary structure is computed only once at the onset of a simulation.

2.1.2 Thermal evolution

Heat sources include both radiogenic heat and heat from accretion, the two sources responsible for nearly all the heat trapped inside the Earth. A lower fraction of radiogenic heat implies a lesser dependence of mantle temperature on planet size and, especially, age (Kite et al., 2009). We factor accretional heating into the planet's initial temperature at mid-mantle depth, T_{m0}, following Canup et al. (2021):

$$T_{m0} = T_{surf0} + 0.6 \times 4\ h\ \chi\ G\ \pi\ \rho\ r_p^2/(3C_p) \quad (1)$$

Table 2. Radionuclide properties. Abundances pertain to the terrestrial planets of the Solar System and are given at the present day, 4.57 Gyr after the birth of the Solar System. The default abundances are those of Turcotte and Schubert (2002).

Property	^{40}K	^{232}Th	^{235}U	^{238}U	Reference	Notes
Half-life (Gyr)	1.26	14.0	0.704	4.47		
Heating rate (μW per kg nuclide)	29.2	26.4	569	94.6		
Abundance	18.0	51.9	0.10	14.2	Lyubetskaya and Korenaga (2007)	Low end-member
(ppb by mass)	36.9	124.0	0.22	30.8	Turcotte and Schubert (2002)	Highest heating
	30.7	84.1	0.15	21.0	Ringwood (1991)	Intermediate heating
	22.8	62.6	0.12	17.2	Lyubetskaya and Korenaga (2007)	Low heating
	28.8	79.5	0.15	20.15	McDonough and Sun (1995)	Intermediate heating

Here, T_{surf0} is an initial surface temperature, h is the fraction of impactor kinetic energy retained by the planet, χ is the ratio of the impactor velocity relative to the escape velocity from the accreting planet, G is the gravitational constant, r_p is the planet's final radius, and C_p is its bulk-averaged heat capacity, taken to be that of the mantle. Volume averaging leads to the factor of 0.6. The parameters χ and especially h are not well constrained. For the Earth, simulations of the Moon-forming impact suggest that the temperature of silicates reached 3000 to 6000 K (Canup, 2004), which necessitates $h\chi \approx 0.2$. We thus adopt this value for the $h\chi$ product, which corresponds to 20% energy retained for average impactor velocities equivalent to the Earth's escape velocity of 11.2 km s^{-1}, and noting that basing such a value on the Moon-forming impact may not be representative of other Earths that did not experience such an impact. The higher accretional heating experienced by larger (higher-R) planets tends to cause early vigorous convection; the heat thus eliminated leads to these planets having counter-intuitively lower lithospheric heat fluxes than an Earth-sized planet in the first 0.5 to 1 Gyr after accretion. Past 2 Gyr, the imprint of accretional heating on thermal evolution vanishes and thermal evolution is dominated by the balance of radiogenic heating and convective or conductive cooling, with larger planets having a hotter mantle and higher heat fluxes (see Fig. 5c in Section 3).

Because radiogenic elements tend to partition with silicates rather than metals, heat production is assumed to take place solely in the mantle. Radionuclide abundances depend on the bulk composition of the accreted material; we allow for user selection from different sets of literature values (Table 2). Canonically, the abundances of Turcotte and Schubert (2002) are assumed (Table 2); the lack of dependency of these values on a planet's bulk composition is discussed in Section 4. Short-lived radionuclides are ignored since the terrestrial planets have been thought to form after many short-lived radionuclide half-lives (Walsh & Levison, 2019), although recent models implying formation within just a few million years may make short-lived radionuclides relevant early in the planet's history (Bhatia & Sahijpal, 2016, 2017; Saito & Kuramoto, 2018; Johansen et al., 2021). The radiogenic power per unit mass H (W kg^{-1}) is expressed as:

$$H = \sum_{i=1}^{4} H_0(i) e^{-ln(2)\ t/t_{1/2}} \tag{2}$$

where $i = 1 - 4$ are the four main long-lived radioisotopes (^{40}K, ^{232}Th, ^{235}U, ^{238}U), H_0 is the product of a radionuclide's specific heating rate with its mass fraction in mantle material at the time the first planet-building solids condense – 4.57 billion years (Gyr) ago for the Solar System –, $t_{1/2}$ is its half-life, and t is time.

The thermal profile from the surface to the base of the crust is calculated as follows. First, a mid-mantle temperature T_m is calculated at each time step with the assumptions of Kite et al. (2009) (e.g., whole-mantle convection), except thermal equilibrium is not assumed:

$$\frac{dT_m}{dt} = H/C_p - \frac{k}{\rho C_p}\ Nu\ (T_m - T_{ref}) \left(\frac{2}{r_{BDT} - r_c}\right)^2 \tag{3}$$

with the Nusselt number (dimensionless ratio of total heat flux to conductive heat flux) given by $Nu = (Ra/Ra_{cr})^{\beta}$. The Rayleigh number Ra is itself given by:

$$Ra = \frac{g\ \alpha\ (T_m - T_{ref})\ (r_{BDT} - r_c)^3}{\kappa\ \nu} \tag{4}$$

Here, k is the thermal conductivity, T_{ref} is the surface temperature T_s in the plate tectonics regime, or the temperature at the base of the lithosphere (see equations 5 and 6) in the stagnant lid regime, r_c is the radius of the core-mantle boundary, r_{BDT} is the ra-

dius of the brittle-ductile transition (BDT), g is the gravitational acceleration, α is the thermal expansivity, $\kappa = k/(\rho C_p)$ is the thermal diffusivity, and ν is the temperature-dependent kinematic viscosity. T_m, g, and ν are evaluated halfway between r_c and r_{BDT}.

The radius of brittle-ductile transition r_{BDT} is that at which the temperature T_{BDT} and pressure P_{BDT} are such that the brittle and ductile strengths of mantle material are equal. It is found by using the previous time step's P_{BDT} and solving for T_{BDT} using a combined binary and Newton-Raphson search (Press et al., 1992). The brittle strength is given by $0.85P$ at low pressure ($P < 200$ MPa) and $0.6P + 50$ MPa at $P > 200$ MPa (Byerlee, 1978). The ductile strength is the ratio of the viscosity (see below) to the time step.

$Ra_{cr} \approx 10^3$ is the critical Raleigh number. We adopt $Ra_{cr} = 1707.762$ from Reid and Harris (1958). We also adopt $\beta = 1/3$, relevant to an isoviscous convective layer (Solomatov, 1995); the viscosity variation with pressure and temperature across the mantle may warrant values closer to 1/4 (Moresi & Solomatov, 1995; Deschamps & Sotin, 2000). Since that viscosity variation is not well constrained, especially for mantle compositions that differ from Earth's, it may make sense to vary β between 1/4 and 1/3; but we find that varying planet mass provides a sufficient range of thermal evolutions for the purposes of this study.

The viscosity of Earth's mantle is assumed non-Newtonian, although this is uncertain (Deschamps & Sotin, 2000). The viscosity is a parallel combination of those obtained with the diffusion and dislocation creep flow laws for olivine given in Table 3 of Korenaga and Karato (2008), with stress equated to lithostatic pressure and the choice of dry (default) or wet mechanism left as a user input.

Based on the mid-mantle temperature T_m, a temperature profile is computed with radius r from the surface to the core. This profile is assumed to have two parts: an adiabat section in the asthenosphere, where heat transfer is convective, and a conductive section in the lithosphere, the upper and only thermal boundary layer since the fluid is radiogenically heated from within (Turcotte & Schubert, 2002). This boundary layer (Fischer et al., 2010) is formally distinguished from the brittle layer ($r > r_{BDT}$), but in practice the two have similar thickness. The temperature profile is computed as $T(r) = min[T_{adiab}(r), T_{upbnd}(r)]$, with:

$$T_{adiab}(r) = T_m - \alpha\ g\ T_m[r - 0.5(r_{BDT} + r_c)]/C_p \tag{5}$$

$$T_{upbnd}(r) = T_m + (T_s - T_m)\ erfc\left[\frac{r_{BDT} - r}{2}\sqrt{\frac{2\ v_{conv}}{\kappa(r_{BDT} - r_c)}}\right] \tag{6}$$

Equation 5 is equation 4.254 of Turcotte and Schubert (2002), evaluated at the mid-mantle depth halfway between r_c and r_{BDT}; see also Katsura et al. (2010). Equation 6 is equation 6.347 of Turcotte and Schubert (2002), evaluated at the lateral midpoint between upwelling and downwelling regions of a convective cell (whose width and height are equal). In equation (6), $erfc$ is the complementary error function, and the convective velocity v_{conv} is computed as in equation 6.379 of Turcotte and Schubert (2002):

$$v_{conv} = 0.354\ \kappa\ Ra^{1/2}/(r_{BDT} - r_c) \tag{7}$$

which is appropriate for a fluid heated from within. A corresponding convection timescale is $t_{conv} = (r_{BDT} - r_c)/v_{conv}$.

The lithospheric thickness z_{Lith} is the depth at which $T_{adiab} = T_{upbnd}$. At the first time step, the temperature profile is computed using the same equations (5) and (6), initializing $r_{BDT} = r_p$ and $v_{conv} = (r_p - 100\ \text{km} - r_c)/10\ \text{Myr}$.

The sensitivity of temperature profiles to mid-mantle depth and rheology for a 1-$M_\oplus$ planet is shown in Fig. 2. A hotter mantle results in a thinner lithosphere, and so does a wet olivine rheology, whose lower resulting viscosities result in more vigorous convection. For the adopted olivine rheologies, mantle temperatures of 2400-2500 K result in a profile that fits constraints for the Earth (Fischer et al., 2010).

The tectonic mode is determined by comparing the yield stress, equated to the brittle (and ductile) strength at the BDT, with the convective drive stress ν/t_{conv}. If the drive stress exceeds the yield stress, plate tectonics proceed; otherwise the planet is assumed to have a stagnant lid. This very rough determination requires viscosities above $\sim 10^{27}$ Pa s for plate tectonics to take place, which is not achieved in our simulations. The tectonic mode only has a minor effect on equation (4) but can significantly affect seafloor weathering, as investigated in the companion paper.

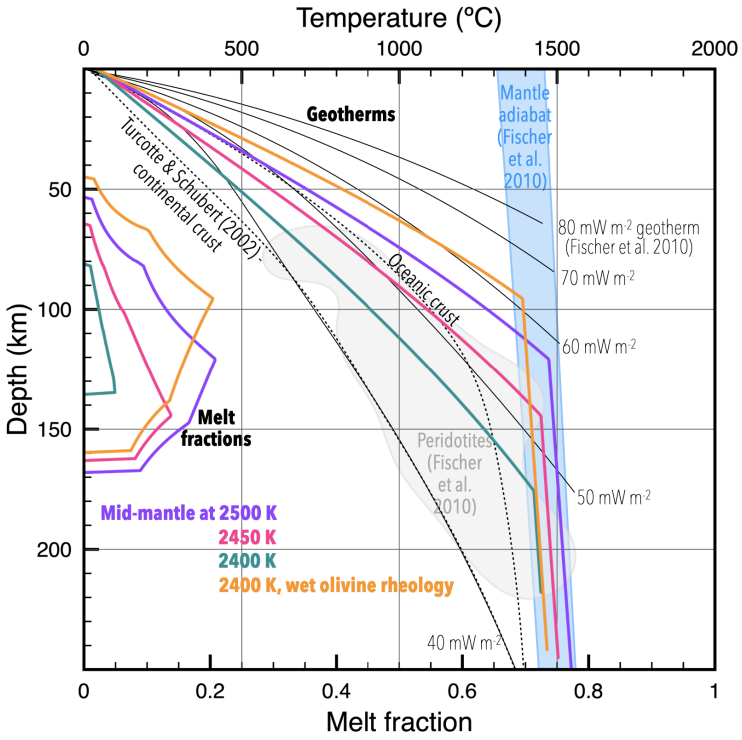

Figure 2. Validation of the melting and outgassing code with present-day Earth. Geotherms (temperature-depth profiles; top x-axis) for a 1-$M_\oplus$ planet are overlain on constraints for Earth's geotherm from analyses of mantle peridotites and measurements of surface heat flux (Turcotte & Schubert, 2002; Fischer et al., 2010). Also shown are melt fraction-depth profiles (bottom x-axis).

2.1.3 Outgassing carbon flux

The outgassing flux, in mol s^{-1}, is assumed to be given by:

$$F_{outgas} = \frac{M_{melt}\ f_{C,magma}}{M_C\ t_{conv}} \tag{8}$$

where M_{melt} is the total mass of melt integrated over depth, $f_{C,magma}$ is the fraction of the melt mass that exsolves as carbon gas, and M_C is the molar mass of CO_2.

To obtain M_{melt}, a mantle melt fraction is computed as a function of depth using the *alphaMELTS* command line implementation of the *MELTS* code (Ghiorso & Sack, 1995; P. M. Antoshechkina & Asimow, 2010; P. M. Antoshechkina et al., 2010; P. Antoshechkina & Asimow, 2018). A specified oxide composition (see Table 4 in Section 3) is provided to *alphaMELTS*, along with settings instructing computation of chemical equilibrium along the above-determined temperature profile, from the surface to the depth at which $P = 10$ GPa. The *MELTS* model is valid for $P < 3$ GPa, and *alphaMELTS* allows (potentially unreliable) calculations beyond this limit up to 4 GPa. Calculations show that there can still be partial melting at 4 GPa. In this case, our model implementation extrapolates linearly the melt fraction trend over the 5 gridpoints closest to 4 GPa, as determined with *alphaMELTS*, to higher pressures until the melt fraction is zero. Based on comparison with an analytical melting model for Earth's upper mantle composition (McKenzie & Bickle, 1988), for which the melt fraction decreases to zero with depth (pressure) faster than linearly, this may slightly overestimate the amount of melt at high pressure. However, these amounts tend to be small relative to M_{melt}.

For the temperature profiles of Fig. 2, the rates of crustal generation from all melt, $M_{melt}/(4\pi\ r_p^2\ \rho_{melt}\ t_{conv})$ with the melt density ρ_{melt} obtained from *alphaMELTS*, are 30.1 ($T_m = 2500$ K), 11 ($T_m = 2450$ K), 1.23 ($T_m = 2400$ K), and 47 m Myr^{-1} ($T_m = 2400$ K, wet rheology) compared to Earth's estimated 40 m Myr^{-1} (Kite et al., 2009). These illustrate a trade between best reproducing Earth's temperature profile with depth (profiles with thicker lithosphere) and best reproducing its rate of crust generation (profiles with thinner lithosphere).

On modern Earth, the magma CO_2 content $f_{C,magma}$ has been variously reported to be 0.03–1 mass% (Hekinian et al., 2000; Jones et al., 2018) in mid-ocean ridge basalts, 0.1–0.65 mass% in ocean island basalts that also possibly approximate Archean Earth

erupted material (Gerlach & Graeber, 1985; A. Anderson, 1995; Hartley et al., 2014), and 0.004-0.15 mass% in back-arc volcanism (Cioni, 2000; Saito et al., 2001; Wade et al., 2006; Blundy et al., 2010). Adopting a canonical abundance of 0.2 mass%, which is within those ranges, yields an outgassing flux similar to that of modern Earth for a 1 Earth-mass, 4.57 Gyr-old planet whose upper mantle has a mid-ocean ridge basalt composition (see Fig. 5 in Section 3).

Outgassed carbon can be speciated into CO_2 and CH_4, with the relative fraction of methane f_{CH4} left as a user input and constant through a simulation. We approximate $f_{CH4} = 0$ for modern and Archean Earth cases, and $f_{CH4} \geq 0.5$ for more metal-rich planetary mantles. For context, the redox state of Hadean Earth magmas was near the fayalite-magnetite-quartz (FMQ) redox buffer (Trail et al., 2011), but a higher proportion of submarine (i.e., high-pressure) volcanism would have affected the composition of the erupted gases (Gaillard et al., 2011), with low (atmospheric)-pressure outgassing likely to be uniformly near FMQ-2 over a range of body sizes, assuming a similar solar-system-like bulk basaltic composition for rock-metal bodies (Gaillard & Scaillet, 2014). In this case, the prime carbon gas erupted is CO_2 (Gaillard & Scaillet, 2014). For undifferentiated or more metal-rich objects, at 1 bar, the predominant carbon gases are CH_4 below 750 K and CO above 750 K (Schaefer & Fegley, 2017).

2.2 Continental weathering

2.2.1 Geochemical kinetics

Weathering describes the physicochemical process which modifies rocky surface landforms by its physical and chemical interaction with fluids having solubilized atmospheric material. As fluids are usually richer in carbon than rock, weathering reactions tend to result in transfer of carbon from the fluid to the rock. A relevant reaction is (Urey, 1952):

$$\underset{\text{wollastonite}}{CaSiO_3} + CO_2(aq) = \underset{\text{calcite}}{CaCO_3} + \underset{\text{silica}}{SiO_2} \tag{9}$$

where (aq) indicates CO_2 in its aqueous form. The fluid-rock setting can be subaerial crust exposed to rain or running water (continental weathering), or suboceanic crust in contact with ocean water (seafloor weathering).

Table 3. Key model parameters for calculating carbon fluxes. Fluxes in mol m^{-2} s^{-1} can be obtained by dividing F_i by $4\pi r_p^2$. [a] User-specified inputs. [b] User-specified input via river runoff rate.

Parameter	Symbol	Value	Units	Notes and references
Outgassing				
Outgassing flux	F_{outgas}		mol s^{-1}	From equation (8)
Mass of mantle melt integrated over depth	M_{melt}		kg	From *alphaMELTS*
Magma carbon fraction [a]	$f_{C,magma}$	0.002	kg kg^{-1}	
Relative fraction of C outgassed as CH_4 [a]	f_{CH4}		kg kg^{-1}	0 for Modern and Archean Earth
				≥ 0.5 for chondritic mantle
Continental weathering				
Continental weathering flux	F_{contw}		mol s^{-1}	From equation (11)
Rainfall rate [b]	p	0.7	m yr^{-1}	Broecker and Peng (1982)
Fresh- and seawater density	ρ	1000	kg m^{-3}	
Areal fraction of planet covered by land [a]	L		–	0.29 for Earth
Freshwater:rock mass ratio	$4\pi r_p^2\ L\ p\ \rho / M_{rock}$	5000	kg kg^{-1}	Martin and Meybeck (1979)
Molalities of dissolved species in rivers	$m_{i,river}$		mol kg^{-1}	From *PHREEQC* kinetic calculation
Continental weathering				
Seafloor weathering flux	F_{seafw}		mol s^{-1}	From equation (13)
Mass of surface ocean [a]	M_{ocean}	1.4×10^{21}	kg	
Hydrothermal circulation timescale	t_{circ}	10^7	yr	Mottl (1983); Kadko et al. (1995)
Length of plate boundaries	L_{plate_ridges}		m	$1.5 \times 2\pi r_p$ for modern Earth
where seafloor is created				$(4.5 - 7.5) \times 2\pi r_p$ for Archean Earth
Depth of fracturing below seafloor	z_{crack}	6	km	Vance et al. (2007)
Molalities of dissolved species in the ocean	$m_{i,ocean}$		mol kg^{-1}	From *PHREEQC* and eq. (14)
River water mass flowed to ocean in a time step	M_{river}		kg	
Carbon incorporated in the crust	ΔC_{reac}		mol	From equation (16)
Atmospheric evolution				
Net carbon flux	F_C		mol s^{-1}	From equation (17)
{Atmosphere+ocean} reservoir	RC_{atm+oc}		mol	
Mantle reservoir	RC_{mantle}		mol	
Time step [a]	Δt		s	Adapted based on RC_i and F_C
Surface pressure [a]	P_{surf}		Pa	Varies during simulation
Surface temperature [a]	T_{surf}		K	Varies during simulation
Number of moles of gas in atmosphere	n_{air}		mol	
Atmospheric mixing ratios [a]	x_i		–	$i = CO_2$, CH_4, N_2, O_2, H_2O;
				vary during simulation
Atmospheric volume	V_{atm}		m^3	Held constant

In planetary-scale models of the carbonate-silicate cycle, continental weathering fluxes are usually assumed to vary with temperature as an Arrhenius law, with runoff (the amount of rainwater involved in weathering reactions and that eventually transports dissolved or particulate surface rock to the ocean), and with atmospheric CO_2 partial pressure. The variation with the latter two parameters is usually expressed as power law deviations from measured Earth values, as in equations 8a, 2, and 1, respectively, of Sleep and Zahnle (2001),

In natural systems, crustal materials are composed of a variety of minerals that all react with carbon-bearing fluids at different rates. To capture the effect of surface composition on reaction rates, new power laws would have to be determined for every surface composition, an impractical challenge. Instead, we opt to compute reaction rates and corresponding continental weathering fluxes from first principles, based on the results of simulations of water-rock interaction through time using the `KINETICS` functionality of the *PHREEQC* software (Parkhurst & Appelo, 2013). *PHREEQC* database and example input files are provided as supplementary material to this article in a Zenodo repository, and data and input compositions are described below.

Chemical reactions, including those involved in continental weathering, proceed at a rate that depends on numerous factors such as temperature, the extent of chemical disequilibrium, concentrations of species such as H^+ (pH), mineral surface properties (Pokrovsky & Schott, 1999), and the action of catalysts. For the latter two processes, a thorough understanding is lacking for a comprehensive set of relevant rock species. The dependence on temperature and composition is better understood, but experimental data have been compiled only for a subset of species that are abundant at Earth's surface (Palandri & Kharaka, 2004). As a result, the calculation of reaction rates is typically captured into a simplified form, fitted to experimental measurements, such as (Palandri & Kharaka, 2004):

$$\frac{dm}{dt} = -\mathrm{SA}\ A\ e^{-\frac{E}{R(T-T_0)}}\ a_{H^+}^n\ (1-\Omega^p)^q \tag{10}$$

Here, m represents the concentration (molality, in moles of species per kg of water solvent) and dm/dt its change over time, SA the surface area available for reaction, E an activation energy, R the gas constant, T the temperature (which influences reaction rates via an Arrhenius law), and T_0 a reference temperature, usually 298.15 K. Ω is a mea-

sure of chemical disequilibrium, equal to Q/K, where $Q = \prod_i a_i^{\nu_i}$ is the product of the species' thermodynamic activities a_i, scaled geometrically by their stoichiometric coefficient ν_i (negative for reactants, positive for products), and $K(T, P)$ is this product when the reaction reaches equilibrium (G. M. Anderson, 2005). K is termed the reaction constant, but depends on temperature T and pressure P. The magnitude of Ω hinges both on the bulk initial compositions of the fluid (e.g., carbon content) and rock, and on how far toward equilibrium the reaction has progressed. The constant A and the exponents n, p, and q are determined experimentally; here, p and q are both approximated to 1 for all species (Palandri & Kharaka, 2004).

Reaction constants K are obtained from the *core10.dat* thermodynamic database described in Neveu et al. (2017), with data from references therein, distributed with *PHREEQC* at https://wwwbrr.cr.usgs.gov/projects/GWC_coupled/phreeqc. For this study, we have augmented the database with kinetic rates for 56 solids compiled by Palandri and Kharaka (2004) and references therein. These include quartz and silica, as well as mineral species in the feldspar, olivine, garnet and other orthosilicates, cyclosilicate, pyroxene, pyroxenoid, amphibole, mica, clay and other phyllosilicates, oxide, hydroxide, carbonate, sulfate, sulfide, and halide groups.

Not all solids need be part of the reacting crust, but all are allowed to form in a simulation. One exception is quartz, included in weathering simulations involving modern Earth and the solar system surfaces of Table 5, but not allowed to form in those involving the surface composition of Archean Earth. This is because quartz is not reactive on relevant timescales (residence time of rain and river water on land) and as such tends to make the system of differential equations (10) too stiff for *PHREEQC*'s implementation of the `CVODE` solver (Cohen et al., 1996) to handle, preventing these simulations from proceeding.

The starting continental crust (Table 5) and rainwater fluid compositions are provided as inputs to *PHREEQC*. The composition of rainwater, including its carbon content, is set to be equilibrated with the atmospheric composition, assuming that the atmosphere is an infinite reservoir. Atmospheric N_2 and its dissolved form are assumed to be inert.

A fluid:rock mass ratio of about 5000 is canonically assumed, although the diversity of terrains on Earth points to much variation from this global mean. This ratio is

based on a reference river runoff rate for Earth of 0.665 mm day^{-1} (Edson et al., 2012), which corresponds to a rainfall rate $p = 0.7$ m yr^{-1} minus evaporation of 65% of the rainwater from rivers (Broecker & Peng, 1982; Martin & Meybeck, 1979). Multiplying by land surface area $4\pi r_p^2\ L$, with L the fraction of planet area covered by land ($L = 0.29$ for Earth), and fluid density $\rho \approx 1000$ kg m^{-3} yields a rainfall mass rate $4\pi r_p^2\ L\ p\ \rho = 1.0{\times}10^{17}$ kg yr^{-1}. The mass of parent rock affected by weathering at the continent surface drained by rivers to the ocean is estimated to be $M_{rock} = 21.1 \times 10^{12}$ kg yr^{-1} in Table V, footnote 3 of Martin and Meybeck (1979). This yields a fluid:rock ratio $4\pi r_p^2\ L\ p\ \rho / M_{rock} = 4918$. The ratio is proportional to p but insensitive to $4\pi r_p^2\ L$ since M_{rock} too is proportional to this term. In our modern and Archean Earth simulations, the fluid:rock ratios are 5000 and 4944, respectively.

2.2.2 Estimating continental weathering carbon fluxes

The *PHREEQC* simulation yields fluid and mineral abundances as a function of reaction time, assuming a chemically closed system (no removal of reactants or products). In the full model (Fig. 1), all solutes are delivered to the ocean where they accumulate and, once saturation is reached, form carbon-bearing minerals that upon subduction transfer carbon from the {atmosphere+ocean} reservoir back to the mantle reservoir (Section 2.3). This approach provides a level of chemical realism not achieved with treatment of distinct continental and seafloor weathering fluxes of carbon, but does not single out the continental contribution to the weathering flux and its dependency on surface composition.

For the purposes of this study, we therefore calculate a continental weathering flux F_{contw}, in mol yr^{-1}, of dissolved carbon that can be sequestered in minerals based on amounts (molalities) $m_{i,river}$ of Ca, Mg, and Fe cations in mol per kg of runoff water after a reaction time equal to the mean residence time of rainwater on land, about 10-15 years on modern-day Earth (Begemann & Libby, 1957; Chahine, 1992). The flux is then:

$$F_{contw} = \sum_i\ j\ m_{i,river}\ 4\pi r_p^2\ L\ p\ \rho \tag{11}$$

Here, i is a summation index on all combinations of aqueous Ca, Mg, Fe, arising from the dissolution of silicate, carbonates, sulfates, and sulfides present in the system. The

stoichiometric integer j is equal to the balance of positive and negative charges among the ions (other than H^+ and OH^-) arising from the dissolution of these minerals: +1, +2, 0, and −2 for carbonates, silicates, sulfates or pyrrhotite, and pyrite, respectively. Indeed, their dissolution yields a doubly charged cation plus, respectively, HCO_3^-, aqueous SiO_2, SO_4^{2-}, or 2 SO_4^{2-} at the river and ocean pH and oxidation conditions of modern Earth (Berner et al., 1983). The contribution of Na and K cations is neglected because their bicarbonate salts are too soluble to sequester carbon. Each excess positive charge can combine with HCO_3^- or 1/2 SO_4^{2-} from rainwater. Twice the rainwater SO_4^{2-} flux is thus removed from the total excess positive charges to obtain F_{contw}.

While this approach to quantifying continental weathering flux provides a basis for determining its sensitivity to surface composition, it is inadequate if the atmosphere, surface, and ocean compositions lead to a predominant dissolved carbon species with a different charge than bicarbonate, such as dissolved CO_2 (carbonic acid, no charge) or carbonate CO_3^{2-} (doubly charged anion) at ocean pH lower than 5 or greater than 10 at Earth surface T and P, respectively, or dissolved organic carbon or CH_4 (no charge) at reducing conditions. Those cases warrant use of the full model of Fig. 1.

2.2.3 Validation: modern Earth

We validate and calibrate *PHREEQC* kinetic simulations of continental weathering at 288 K and 1 bar with estimates of river abundances of major rock-forming elements (Martin & Meybeck, 1979) and corresponding continental weathering fluxes F_{contw} for modern Earth (Berner et al., 1983; Lerman & Wu, 2006; Colbourn et al., 2015) at reaction (residence) times of 10-15 years (Begemann & Libby, 1957; Chahine, 1992). Abundances of major rock-forming elements in rivers are obtained by dividing simulated molalities $m_{i,river}$ by $1 - 0.65 = 0.35$ to account for 65% evaporation on land (Broecker & Peng, 1982).

A felsic crust composition (see 'Earth (modern)' column of Table 5 in Section 3) is set by adjusting starting abundances of quartz; Na-, Ca-, and K-feldspars; phyllosilicates (annite, phlogopite, daphnite); and hornblende (anthophyllite and tremolite) to match mineral volume fractions from Nesbitt and Markovics (1997) and oxide mass fractions from Rudnick and Gao (2003) within 10%. To this, we add calcite and dolomite (which rapidly and fully dissolve) to obtain carbonate contributions of Ca and Mg cations

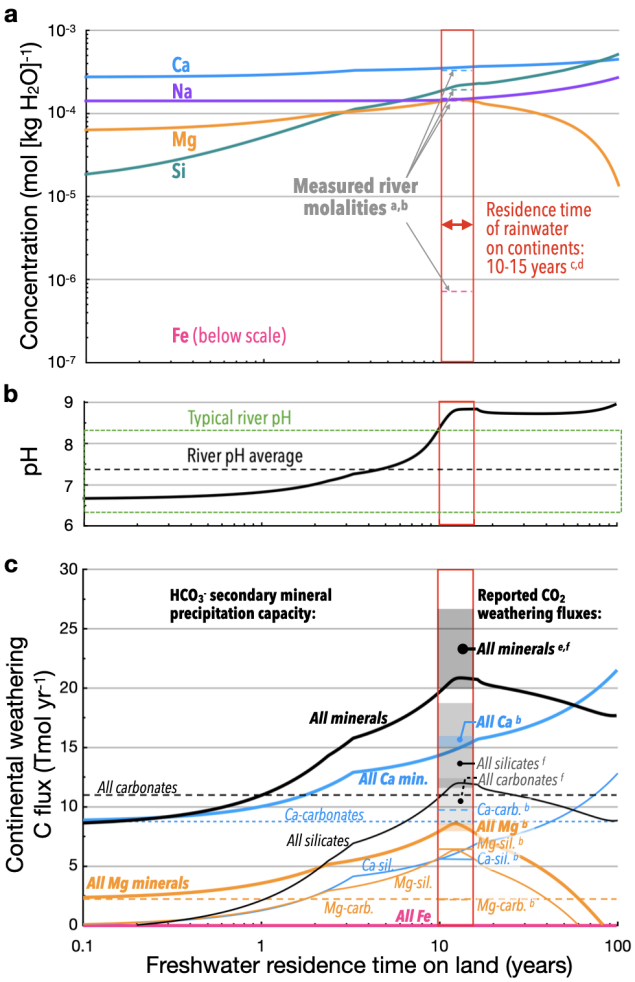

Figure 3. Validation of continental weathering model against modern Earth average river compositions and weathering fluxes. **a.** *PHREEQC* simulated molalities $m_{i,river}$ of dissolved Na, Mg, Si, Ca, and Fe (solid lines) at 288 K and 1 bar, divided by (1 − 0.65) to account for 65% evaporation, compared to measured averaged river abundances (dashed lines) at relevant residence times of 10 to 15 years (red window). **b.** Corresponding river pH. **c.** Resulting total net flux (thick black line), obtained from the $m_{i,river}$ shown in (a) using equation (11), and contributions to this flux from various mineral groups (subsets of the terms summed in equation 11), compared to literature ranges (shaded bands and lines inside the red box). The total flux curve is corrected to exclude about 2.4 Tmol yr^{-1} of cation fluxes, which are assumed to react with the corresponding flux of sulfate from rainwater and sulfide weathering generated by the model (Berner et al., 1983). Because this approach does not attribute the total sulfate flux contribution to specific mineral groups, the curves showing mineral group contributions include this sulfate flux contribution and therefore slightly overestimate the contribution of each group to the CO_2 drawdown flux. Another 2.4 Tmol yr^{-1} of sulfate arises from weathering of sulfate minerals, chiefly gypsum, but the sulfate and calcium arising from it are not shown here as together they do not affect the charge balance. [a] Martin and Meybeck (1979). [b] Berner et al. (1983). [c] Begemann and Libby (1957). [d] Chahine (1992). [e] Lerman and Wu (2006). [f] Colbourn et al. (2015).

in the ranges given by equations 10 and 17 of Berner et al. (1983) and by Table S1 of Colbourn et al. (2015) and references therein. The added amounts correspond to 5.3 vol% of exposed land, within the $4.2 - 8.8$ area% range estimated for the past 500 Myr on Earth, $(6.2 - 13)\times10^6$ km^2 (Kiessling et al., 2003), although part of this area is underwater on continental shelves. We also add sulfate (gypsum) and sulfide (pyrite) at abundances that match their estimated modern contributions to river sulfate; see p. 645 of Berner et al. (1983).

The liquid composition is set to be equilibrated with partial pressures of 0.78 atm of N_2, 0.2 atm of O_2, and 4000 μatm of CO_2. The CO_2 partial pressure, within the several thousand μatm range measured for large rivers (Cole & Caraco, 2001), reflects supersaturation relative to the atmosphere (pre-industrial pCO_2 of 280 μatm) due to biological respiration of biogenic reduced carbon from soil (Rasilo et al., 2017; Lynch et al., 2010). The liquid also comprises 8 μmol kg^{-1} of sulfate, corresponding to the estimated 0.8 Tmol yr^{-1} pre-industrial sulfur contribution from outgassing and atmospheric cycling (Berner et al., 1983).

PHREEQC calculations with this input reproduce both a set of average cation concentrations in Earth rivers (Fig. 3a) and reported ranges of the weathering flux, including contributions from various mineral groups (largely Ca- and Mg- silicates and carbonates) (Fig. 3c). The computed river water sulfur abundance (constant with time) of 6.9×10^{-5} mol kg^{-1} S, which corresponds to 6.6 mg kg^{-1} SO_4^{2-}, is in the reported range of $5.19 - 11.2$ mg kg^{-1} SO_4^{2-} of Lerman et al. (2007) and references therein.

A few differences stand out. First, in the simulation nearly all Fe is in minerals. Measured dissolved river Fe molalities may be non-negligible only because of (biogenic) organic complexation (Gibbs, 1975), and can only be matched in a simulation if precipitation of Fe oxides is prevented. Second, the simulated river pH past 10 years of interaction is at the high end of typical measured river values (Fig. 3b). Third, the Ca-carbonate (calcite) contribution to weathering flux is lower than estimated by Berner et al. (1983). However, the Mg-carbonate contribution matches their estimate and the total carbonate contribution is in the middle of the range reported in Table S1 of Colbourn et al. (2015).

To convert dissolved abundances to weathering fluxes we have assumed $L = 0.29$, irrespective of whether this land is drained by rivers to the oceans (i.e., exorheic). Exorheic areas have been variously estimated as comprising half to two thirds of the con-

tinental area on modern Earth (Lerman et al., 2007). Excluding Greenland and Antarctica, on which short-term weathering is impeded by the ice cover, but including endorheic areas in the ratio of surface water reservoirs to riverine fluxes (Chahine, 1992) results in $L = 0.26$, thus lowering fluxes of Fig. 3c by 10%.

In this calculation, we altered the dissolution kinetics of feldspar along the solid solution between Ca (anorthite, fastest dissolving) and Na (albite, slowest dissolving) end-members in order to limit the rate of Ca dissolution. Otherwise, the additional Ca in solution increases the pH, limiting dissolved Mg. We found that attributing 85% of anorthite the kinetic law for labradorite (50-70% anorthite, 30-50% albite) and the other 15% the law for bytownite (70-90% anorthite, 10-30% albite) achieved a suitable balance between dissolved Ca and dissolved Mg as shown in Fig. 3c. We did not change the dissolution rate for albite, assumed to be the end-member's law, but instead controlled the amount of Na in solution with NaCl (see Table 5 in Section 3).

When applying this model to other surface and atmospheric compositions in lifeless conditions, we restore pCO_2 to the atmospheric value, scale the 8 μmol kg^{-1} of dissolved atmospheric sulfur by the ratio of pCO_2 to Earth's modern pCO_2, and retain the 85% labradorite – 15% bytownite kinetic rate law for anorthite. Implicit in the second choice is the simplifying assumption that atmospheric CO_2 and SO_2 co-vary; the model does not explicitly track atmospheric SO_2.

2.3 Seafloor weathering

Seafloor weathering describes the loss of carbon from the {atmosphere+ocean} reservoir to the mantle reservoir. If the planet does not experience plate tectonics, dissolved species delivered by rivers continue to accumulate until saturation is reached and minerals precipitate. If plate tectonics operate, ocean fluids can react with fresh (unreacted) new ocean crust exposed at the seafloor.

In either case, it is sensible to assume that unlike continental weathering reactions, ocean-seafloor reactions proceed to chemical equilibrium. If ocean crust is recycled, the recycling timescale depends, to first order, on the vigor of mantle convection. The current rates of production of oceanic crust are about 20 km^3 yr^{-1} $\approx 2 \times 10^6$ kg s^{-1} on Earth (Cogné & Humler, 2006), with the mantle convecting on a timescale of 10^8–10^9 years. This timescale holds for the larger, younger, or compositionally different planets

in the simulations whose outgassing fluxes are shown in Fig. 5. This is slower than circulation of ocean fluids through fractures or porosity in this crust, which occurs on a timescale $t_{circ} \sim 10^7$ years (Mottl, 1983; Kadko et al., 1995). It is also slower than chemical equilibrium between these fluids and crustal rock: a *PHREEQC* kinetic simulation of reaction between a fluid with modern-day seawater composition from Parkhurst and Appelo (2013) (simplified from Nordstrom et al. (1979)) and mafic crust composition (see Table 5, 'Earth (Archean)' column, in Section 3) shows that chemical equilibrium is reached on timescales of $10^5 - 10^6$ years (Fig. 4). This equilibrium is calculated at the ocean surface temperature (a lower bound), 405 bar (depth of about 4 km), and a water:rock mass ratio of 1 (see below).

The reaction takes place at seafloor pressure and surface temperature, in the approximation of an isothermal ocean. Water-rock reactions at or below the seafloor can, but need not, take place at elevated temperatures relative to that of the ocean. The water:rock ratio by volume is determined by:

$$\frac{V_{fluid}}{V_{ocean\ crust}} = \frac{(M_{ocean}/\rho) \times \Delta t / t_{circ}}{\frac{1-L}{1-0.29}\ L_{plate\_ridges}\ v_{conv}\ z_{crack}\ \Delta t} \tag{12}$$

This ratio is independent of the time step Δt. Here, L_{plate_ridges} is the length of plate boundaries where new seafloor is created (this excludes subduction zones). On modern Earth, this length is about 1.5 times Earth's circumference. We scale it for different mantle convective vigor as $L_{plate\_ridges} = (Ra/2.3\times10^6)^\beta \times 1.5 \times 2\pi r_p$, which is consistent with a linear proportion to the Nusselt number and with a 3 to 5 times greater ridge length in the Archean (Kadko et al., 1995). v_{conv} is the plate velocity, which can simply be equated to the mantle convective velocity (Turcotte & Schubert, 2002), or arbitrarily decreased from that value to simulate more sluggish tectonics as may have been the case at the onset of plate tectonics (Brown et al., 2020). z_{crack} is the depth into the seafloor to which fluid can circulate, with estimates for the present day varying between 600 m (Johnson & Pruis, 2003) and 6 km (Vance et al., 2007) (see also Hasenclever et al. (2014)), with deeper circulation appearing possible if plate velocity is very low (Tao et al., 2020). We adopt $z_{crack} = 6$ km.

The seafloor weathering flux, in moles per unit time, is the difference ΔC_{reac} in the molality of aqueous carbon $m_{C,ocean}$ in the ocean pre- vs. post-reaction (mol kg^{-1}), multiplied by the ocean mass M_{ocean} and divided by the time step:

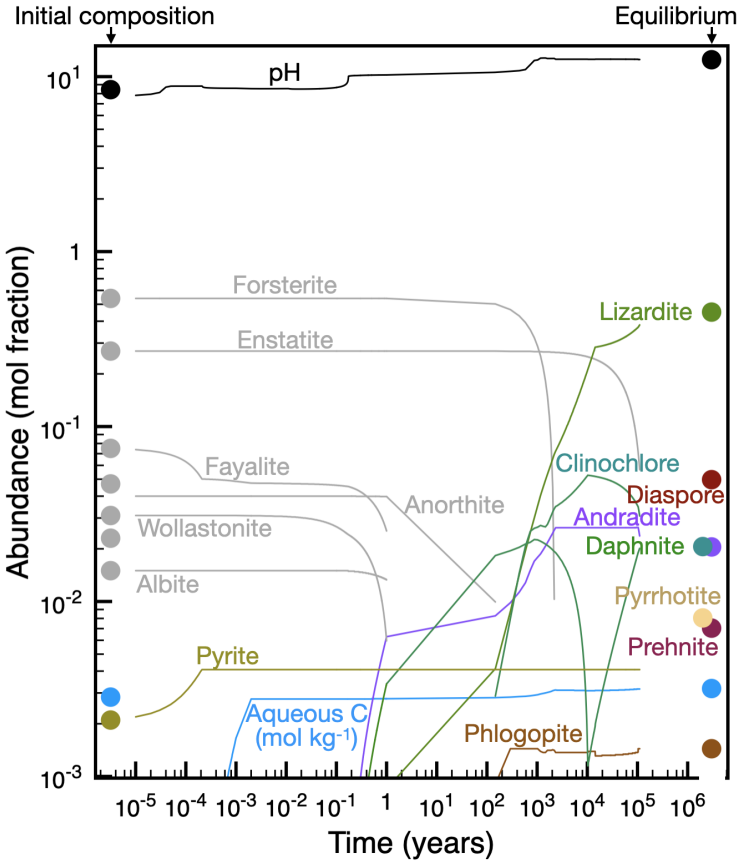

Figure 4. Abundances of minerals and solutes as a function of time (lines) in a kinetic simulation at 288 K and 405 bar of the interaction between seafloor rock and seawater at a mass ratio of 1. These abundances, compared to those computed for an equilibrium simulation (thick dots), indicate that equilibrium is approached at about 10^5 years, although some Al- and S-rich minerals such as, respectively, clinochlore and pyrite have not yet reacted to diaspore and pyrrhotite.

$$F_{seafw} = \Delta C_{reac}\ M_{ocean}/\Delta t \tag{13}$$

The pre-reaction ocean molality $m_{i,ocean}$ of each element is an average of the ocean composition at the previous time step ($m_{i-1,ocean}$) and that of riverine input (molalities $m_{i,river}$), scaled by the relative masses of the ocean and river runoff over a timestep:

$$m_{i,ocean,t} = \frac{m_{i,ocean,t-1}\ M_{ocean} + m_{i,river}\ M_{river}}{M_{ocean} + M_{river}}. \tag{14}$$

M_{ocean} is a user input (default 1.4×10^{21} kg for modern Earth) and is assumed constant with time. The mass of river water M_{river} flowing into the ocean during a timestep is given by:

$$M_{river} = 4\pi r_p^2\ L\ \frac{p}{1 - 0.65}\ \rho\ \Delta t \tag{15}$$

Only a subset $\Delta t/t_{circ}$ of the ocean reacts with the seafloor; the resulting fluid is then mixed back with the rest of the ocean to update the ocean composition. Following this mixing step, mineral precipitation is allowed in case the ocean has become supersaturated; the resulting fluid composition is the ocean composition post-reaction. This allows determination of ΔC_{reac} as:

$$\Delta C_{reac} = m_{C,ocean,post-reaction} - m_{C,ocean,pre-reaction} \tag{16}$$

where $m_{C,ocean}$ refers to the total molality of dissolved carbon, summed over all dissolved carbon species (including but not limited to CO_2, CH_4, HCO_3^-, and CO_3^{2-}).

River-ocean and hydrothermal fluid-ocean mixing simulations are carried out using *PHREEQC*'s `MIX` functionality, which allows consistent tracking of pH and redox conditions through the mixing reactions. The pressure of reaction is adjusted using the `REACTION_PRESSURE` keyword. Fluid-rock equilibria are calculated using the `EQUILIBRIUM_PHASES` functionality, either in the presence of seafloor rock (assumed, e.g., to have the mafic Archean crust composition given in Section 3's Table 5) if plate tectonics occur, or without reactive rock otherwise. In the latter case, transfer of carbon from the ocean to minerals occurs if the ocean composition following riverine input is such that carbon-bearing min-

erals are supersaturated, as expected if the ocean is already in equilibrium with a carbon-bearing atmosphere prior to riverine input.

For an ocean saturated in carbon both before the addition of riverine input and after seafloor interaction and precipitation of any supersaturated minerals, ΔC_{reac} is proportional to Δt. Therefore, F_{seafw} is independent of Δt, as confirmed with simulations involving seafloor weathering with various time steps (see companion paper).

2.4 Net carbon flux and atmospheric evolution

The net flux F_C of carbon between the {atmosphere+ ocean} and mantle reservoirs is the sum of F_{outgas}, the outgassing flux given by equation (8), and F_{seafw} given by equation (13). The latter term accounts for contributions from continental weathering via the term ΔC_{reac} (see equations 14 and 16), and as such represents the effects of both continental and seafloor weathering. If plate tectonics operate, this term is scaled by a fraction f_{arc} (default value 0.25 for Earth) that accounts for partial outgassing of subducted carbon via back-arc volcanism. Thus:

$$F_C = F_{outgas} + (1 - f_{arc})\ F_{seafw}. \tag{17}$$

The {atmosphere+ocean} and mantle reservoirs of carbon, respectively RC_{atm+oc} and RC_{mantle} in mol, are respectively incremented or decremented at each timestep by $F_C\ \Delta t$. A maximum timestep is set as a user input (canonically, 1 Myr) and decreased if needed during a simulation to $0.1 \times min(RC_{atm+oc}, RC_{mantle})/|F_C|$ in order to maintain numerical stability.

At the first time step, RC_{atm+oc} is initialized by specifying initial atmospheric partial pressures of CO_2 and CH_4 and using *PHREEQC* to determine the corresponding (equilibrium) $m_{C,ocean}$. The initial RC_{mantle} is derived from the mantle mass (Section 2.1.1) and the canonical assumption that the mantle comprises 200 ppm C by mass. This is in the inferred range of 20-1800 ppm (Dasgupta & Hirschmann, 2010) and implies depletion by a factor of 10 relative to the abundance of carbon in mantle melt of 0.2% (Section 2.1.3). Thus, there is canonically about 10^3 times more carbon in the mantle than in the {atmosphere+ocean} reservoir (see Fig. 7 in Section 4).

The atmospheric surface pressure P_{surf} and mixing ratios $x_{CO2} = pCO_2/P_{surf}$ and $x_{CH4} = pCH_4/P_{surf}$ are updated at each time step based on F_C and f_{CH4}. This is done by equilibrating the atmospheric and ocean compositions using *PHREEQC* at surface temperature T_{surf} (fixed in this *PHREEQC* calculation) and pressure P_{surf} (modified by this *PHREEQC* calculation based on gas exchange with the ocean). Pre-equilibration conditions are set according to, respectively:

$$\Delta P_{surf} = F_C \ \Delta t \ R \ T_{surf}/V_{atm} \tag{18}$$

$$x_{CO2,t+1} = \frac{x_{CO2,t} \ n_{air} + (1 - f_{CH4})F_C\Delta t}{n_{air} + F_C\Delta t} \tag{19}$$

$$x_{CH4,t+1} = \frac{x_{CH4,t} \ n_{air} + f_{CH4}F_C\Delta t}{n_{air} + F_C\Delta t} \tag{20}$$

where V_{atm} is the atmospheric volume and T_{surf} the surface temperature.

V_{atm} is held constant throughout the simulation, and computed at the first timestep as $V_{atm} = n_{air} \ R \ T_{surf}/P_{surf}$. The number of moles of air n_{air} is initiated as $n_{air} = P_{surf} \times 4\pi r_p^2/(g_{surf} \ M_{air})$, with M_{air} the average atmospheric molar mass (calculated from the user-input atmospheric partial pressures of CO_2, CH_4, N_2, O_2, and H_2O) and g_{surf} the surface gravity. n_{air} is incremented at each time step by $F_C \ \Delta t$.

The model is intended for coupling with models of atmospheric photochemistry and radiative transfer (Kasting & Ackerman, 1986; Kopparapu et al., 2013; Arney et al., 2016; Vidaurri et al., 2022). However, its implementation can be run independently, in which case T_{surf} is computed by summing a term from insolation, which changes over geologic timescales, and a term capturing the atmospheric greenhouse effect. Both terms are parameterized as in Caldeira and Kasting (1992). This parameterization is valid for 10^{-8} bar $< \ pCO_2 \ < \ 10^{-2}$ bar. For standalone simulations, we also roughly parameterize the rainfall rate p as $p \ \propto \ T_{surf}^{1.025}$ (with $p = 0.7$ m yr^{-1} for $T_{surf} = 288$ K), reflecting a roughly 2.5% increase in global mean precipitation on Earth per Kelvin of temperature increase (Allen & Ingram, 2002; Trenberth et al., 2005; Pendergrass, 2020). An example such standalone simulation is provided in Section 4.

2.5 Neglected processes

The ocean mass is approximated as constant over time, even though on Earth it may have increased or decreased by a factor up to about 1.5 over geologic time (Harrison, 1999; Korenaga, 2008; Pope et al., 2012; Laneuville et al., 2018). We do not consider the potential sequestration of carbon species in ice caps or loss to space. Atmospheric speciation, photochemistry, and effects on surface temperature and runoff are not considered in this paper. This model does not differentiate between degassing of primordial vs. subducted carbon.

This model does not explicitly track outgassing chemistry as a function of source depth, degassing transport, and outgassing pressure. While these aspects are thought to impact the redox state of outgassed material, the extent to which they do is debated (Burgisser & Scaillet, 2007; Dasgupta & Hirschmann, 2010). The fO_2 of magmas and associated abundances of gas species in equilibrium with the magma composition could change up to 1.5-2 orders of magnitude upon ascent, due to degassing and pressure effects on volatile exsolution (Burgisser & Scaillet, 2007). However, this variation could go in either direction (toward a more oxidizing or reducing magma), depending on the starting conditions, unless the volatiles are primarily H_2 and H_2O, with little C and S species. Moreover, the findings of Burgisser and Scaillet (2007) applied to Fe-poor (rhyolitic) magmas, but more mafic magmas may provide added buffering capability, decreasing changes in magma redox during ascent.

3 Results

In this section, we describe the sensitivity to planet size and composition of carbon fluxes arising from outgassing and weathering. The sensitivity of the carbon cycle and resulting atmospheric composition on these properties is investigated in the companion paper.

3.1 Geological controls on outgassing

The outgassing fluxes through time of rocky silicate planets with a surface water ocean and a surface temperature similar to Earth's are shown in Fig. 5a as a function of planet mass and upper mantle composition. Planet mass is varied between 0.5 and

653 2 $M_\oplus$, with the same planet-building materials and core mass fraction as in the mod-
654 ern Earth validation simulation shown in Fig. 2 and a dry olivine rheology.

655 Four upper mantle compositions are investigated: mid-ocean ridge basalt (Allan
656 et al., 1989), chondritic (Sanloup et al., 1999), rhyolitic (Pamukcu et al., 2015), and fel-
657 sic (Dolinschi, 2019) (Table 4). These oxide compositions were speciated into mineral
658 compositions assuming an oxidation state corresponding to the FMQ buffer. Varying fO_2
659 to several log units below this buffer did not significantly affect the propensity of these
660 compositions to melt (or, therefore, the outgassing fluxes).

661 Simulations span the time interval between 0 and 5 Gyr after formation, but out-
662 gassing fluxes are computed only after 0.6 Gyr to allow for the initial geodynamic evo-
663 lution to lead to a more steadily evolving mantle temperature and heat flux. The time
664 step in these simulations is 10 Myr, which achieves numerical convergence since climate
665 feedbacks are not tracked for this outgassing flux sensitivity analysis.

666 Outgassing fluxes span 2×10^4 to 6×10^6 mol s^{-1}. They tend to be greater at
667 earlier times and for more felsic compositions. They decrease with increasing planet mass
668 if the mass is greater than $1M_\oplus$, but the mass at which outgassing fluxes peak is lower
669 for the two more felsic compositions: $0.5-0.75M_\oplus$ compared to $1M_\oplus$ for the basaltic
670 (Earth-like) upper mantle composition and $1.5M_\oplus$ for the ultramafic (chondritic) com-
671 position. The outgassing fluxes for the $1M_\oplus$ planets are usually within a few percent of
672 the peak values as a function of planet mass, irrespective of composition; whereas whether
673 the outgassing flux for 0.5-, 0.75-, or 1.5-$M_\oplus$ planets is close to this maximum depends
674 sensitively on composition. For example, for basaltic Earth-like or chondritic composi-
675 tions, outgassing fluxes for 0.5-$M_\oplus$ planets are lower than those of 1-$M_\oplus$ planets by tens
676 of percent at any given time after formation.

677 The general decrease of outgassing fluxes with time is consistent with the global
678 thermal evolution which tends toward lower mantle temperatures and heat fluxes as ra-
679 diogenic heating decreases over time. The decrease spans up to two orders of magnitude
680 between the first billion years after formation and the present day, but with consider-
681 able variability. It is less pronounced for higher-mass planets within the range investi-
682 gated and for more felsic compositions. For 2 $M_\oplus$ planets, the flux first increases to peak
683 at 1 to 2 Gyr after formation before decreasing to 5-Gyr values that are close to fluxes

Table 4. Simulated mantle compositions in mass% oxides: mid-ocean ridge basalt (MORB; Allan et al. (1989) as cited in Ghiorso and Sack (1995)), felsic (Dolinschi, 2019), rhyolitic (Pamukcu et al., 2015), and chondritic (Sanloup et al. (1999) as cited in Taylor (2013)). About 1 mass% or less of SiO_2 was either added or removed from the reported compositions in order for the total to reach 100%. These compositions are free of sub-percent mass fractions reported for Mn, Cr, and K oxides, as P. Antoshechkina and Asimow (2018) advised that including these as major oxides rather than trace elements in MELTS calculations can lead to unpredictable results. The rhyolitic composition's non-negligible K_2O mass fraction (Pamukcu et al., 2015) was added as additional Na_2O. Reported mass fractions of Al_2O and Fe_2O_3 were converted to mass fractions of Al_2O_3 and FeO, respectively, because Al_2O is not part of the MELTS chemical model and MELTS partitions Fe between Fe_2O_3 and FeO during a calculation based on the chosen redox buffer (here, FMQ).

Oxide	MORB	Chondritic	Rhyolitic	Felsic
SiO_2	48.4	48.6	75.6	52.8
MgO	9.1	27.0	0.2	29.2
FeO	8.5	17.5	1.0	12.2
Al_2O_3	17.6	3.6	13.2	2.8
CaO	12.5	2.0	0.8	2.4
TiO_2	1.0	0.1	0.2	-
Na_2O	2.7	1.2	9.1	0.6
P_2O_5	0.1	-	-	-
H_2O	0.2	-	-	-

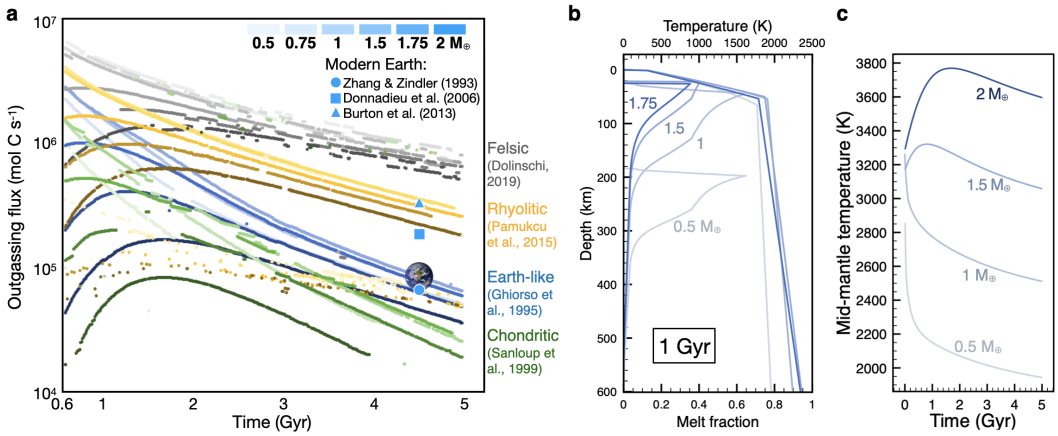

Figure 5. **a.** Effect of planet mass and upper mantle composition on outgassing flux through time. Planet mass is varied between 0.5 and 2 $M_\oplus$ and shown as lighter to darker shade, respectively. Four upper mantle compositions are investigated: mid-ocean ridge basalt ("Earth-like", blue curves), chondritic (green curves), rhyolitic (yellow curves), and felsic (gray curves). The Earth symbol indicates the computed outgassing rate for modeled modern Earth conditions at which the model was validated (Fig. 2); the other three blue symbols indicate literature estimates of this value (Zhang & Zindler, 1993; Donnadieu et al., 2006; Burton et al., 2013). Gaps in curves or (especially for the rhyolitic composition) spuriously low values arise from lack of convergence of *MELTS* calculations at the full set of relevant shallow depths for those particular combinations of composition and mass- and age-dependent geotherm. **b.** Effect of planet mass (pressure-temperature profile) on the extent of melting of an upper mantle of basaltic (Earth-like) composition. **c.** Mid-mantle temperature through geologic time for planets of different masses, all with a basaltic upper mantle.

computed at 0.6 Gyr. For felsic upper mantle compositions, the decrease in outgassing flux does not exceed 1 order of magnitude between 0.6 and 5 Gyr.

At early times, mass has the largest effect on outgassing flux, but past 2 Gyr after formation, the outgassing fluxes become instead more strongly influenced by upper mantle composition. At 0.6 Gyr, the outgassing flux for $\leq 1 M_\oplus$ planets is greater than 10^6 mol s^{-1} for all four upper mantle compositions simulated, whereas the outgassing flux for $2 M_\oplus$ planets is lower than 10^6 mol s^{-1}. Instead, at 4 Gyr, the outgassing flux ranges corresponding to planet masses in the range $0.5{-}2 M_\oplus$ for each of the four compositions simulated no longer overlap: the flux ranges are about $8 - 12$, $3 - 6$, $0.8 -$

693 2, and $0.1 - 0.7 \times 10^5$ mol s^{-1} respectively for the felsic, rhyolitic, basaltic, and chon-
694 dritic mantle compositions.

695 The mass dependence of outgassing flux arises primarily from the influence of planet
696 mass on the geotherm (pressure-temperature profile) and its position relative to the solidus
697 for a given composition. For an Earth-like, basaltic upper mantle composition, planets
698 more massive than Earth have higher internal pressures and a shallower lithosphere-asthenosphere
699 boundary (Fig. 5b). This tends to limit the extent of mantle melting relative to a 1-$M_\oplus$
700 planet. Planets less massive tend to be cooler because of their lower ratio of volume (ac-
701 cretional and radiogenic heat production) to surface area (heat loss). This also limits the
702 extent of mantle melting (Fig. 5b). Thus, melting (and, proportionally, outgassing) is
703 generally maximized for 1-$M_\oplus$ planets.

704 The above analysis applies past 2 Gyr. At earlier times, outgassing is much more
705 suppressed on planets more massive than Earth owing to, counter-intuitively, relatively
706 low internal temperatures and heat fluxes (Fig. 5c). This is because convective heat trans-
707 port is so efficient immediately after formation (due to the need to evacuate the high heat
708 of accretion) that mantle temperatures become uniform enough for the vigor of convec-
709 tion and associated heat flux to drop below those of lower-mass planets. This results in
710 planets whose geotherm seldom crosses the solidus, and therefore in little melting and,
711 proportionally, outgassing. Later on, the heat flux increases back due to radiogenic heat-
712 ing.

713 The compositional dependence of outgassing flux arises from the position of the
714 upper mantle material's solidus curve relative to the geotherm of a planet of given mass
715 and age. The more felsic compositions of Dolinschi (2019) and Pamukcu et al. (2015)
716 have lower melting temperatures; therefore, the degree of melting for a given geotherm
717 crossing their solidus is higher, leading to higher outgassing.

718 ### 3.2 Geological controls on continental weathering

719 The effect of surface composition on continental weathering fluxes of rocky silicate
720 planets is shown in Fig. 6a. The diverse surface compositions simulated are reflective
721 of those of inner solar system planets (Table 5). These simulations were carried out as-
722 suming a 20% CO_2, 80% N_2, 1-bar atmosphere; a 288 K surface temperature; and modern-
723 Earth rainfall rate of 0.7 m yr^{-1} (water:rock ratio $\approx$ 5000). As in Fig. 3c, weathering

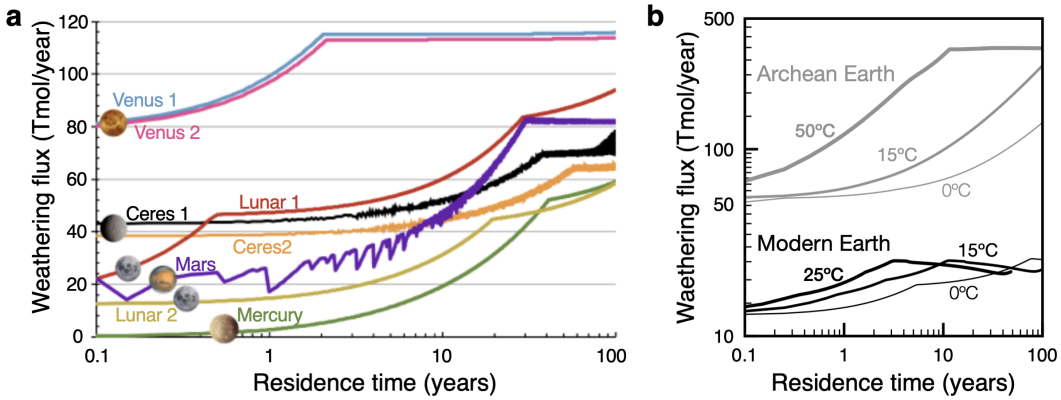

Figure 6. **a.** Continental weathering flux as a function of planet surface composition and residence time of rainwater on land. This flux is expressed as the equivalent cation capacity able to combine with bicarbonate (HCO_3^-) to form mineral precipitates. For each curve, a thumbnail of the planetary surface and labels "1" and "2" indicate the surface composition based on Table 5. The jaggedness in the curves for the Mars- and Ceres-like surface compositions is due to *PHREEQC* having difficulties converging on equilibria involving the precipitation of insoluble oxidized iron minerals. **b.** Dependence of weathering flux as a function of residence time on temperature for surface compositions approximating those of Modern and Archean Earth (Table 5).

fluxes are expressed as the equivalent cation capacity able to combine with bicarbonate (HCO_3^-) to form mineral precipitates.

As shown in Fig. 6a, surface composition has a moderate effect on continental weathering fluxes, which are all on the order of tens of Tmol yr^{-1}. Weathering fluxes are higher if the surface is made of minerals able to rapidly dissolve, such as sulfates (Venus-like surface) and carbonates (Ceres-like surface). The resulting enrichment of river water in cations likely acts as a negative feedback onto the dissolution of other minerals as Ω in equation (10) increases toward 1 (i.e., $Q \rightarrow K$), preventing weathering fluxes from varying by more than about 1 order of magnitude.

Continental weathering fluxes increase with increased continental residence time, because the longer water-rock interaction leads to more mineral dissolution not fully compensated by precipitation of supersaturated minerals. For a given rainfall rate, weathering should thus be more effective on less patchy land.

Continental weathering fluxes also generally increase with temperature (Fig. 6b), as expected from the Arrhenius (exponential) dependence of reaction kinetic rates on the inverse of temperature. Despite this general trend, the relationship is more complex and depends, e.g., on residence time of water on land. For the modern Earth case, if the residence time exceeds 50 years (i.e., for continental masses more consolidated than today), the weathering flux is lower at higher temperatures because mineral formation reactions that consume dissolve cations proceed faster owing both to faster kinetics and to the faster accumulation of river cations (from prior mineral dissolution) to reach mineral saturation. Thus, especially on less patchy land, weathering fluxes may instead be controlled mainly by (proportional to) land area and rainfall.

Expressing weathering flux as the equivalent cation capacity able to combine with bicarbonate (HCO_3^-) to form mineral precipitates requires making the implicit assumption that oxidized carbon is present as bicarbonate, i.e., that the ocean pH is roughly between 6 (below which dissolved CO_2, i.e., carbonic acid, dominates) and 10 (above which doubly charged carbonate dominates). At pH > 10, the oxidized carbon cation trapping capacity would be halved to conserve charge balance; at pH < 6, the trapping capacity of cations would be zero since carbonic acid is neutral. In carbon cycling evolution simulations that combine outgassing, weathering, and ocean-atmosphere equilibrium, the

ocean pH tends to be between 6 and 9 (see Fig. 7 in Section 4 and companion paper), making bicarbonate trapping capacity a reasonable means of evaluating weathering flux.

4 Discussion

Carbon is cycled between the atmosphere, surface, and interior of a planet by outgassing, weathering, and subduction. The balance between fluxes associated with these processes determines the amount of carbon accumulated in the atmosphere-surface and interior reservoirs. The above results enable us to understand how a planet's size and composition affects the intrinsic strength of these fluxes, i.e., of carbon cycle feedbacks. To do so, we have evaluated the magnitude of outgassing and continental weathering fluxes; for the latter, in the specific conditions of Earth's modern-day atmosphere.

4.1 Effect of planet size and composition on continental weathering and outgassing

Our simulations suggest that the efficiency of outgassing and subduction decreases with mass for planets between 1 and 2 Earth masses. This contradicts the findings of Kite et al. (2009) but is in line with more recent work accounting for the effects of high pressure increasing mantle viscosity and thus decreasing its propensity to convect (Stamenković et al., 2012). Here, planet mass is found to influence outgassing in other ways: at lower masses, lower mantle temperatures decrease the degree of melting. At higher masses, higher pressures decrease the degree of melting. We have assumed, as did Kite et al. (2009), that all melt produced reaches the surface, but planet mass may also have an impact on the degree to which intrusive volcanism does not lead to outgassing, proportionally decreasing outgassing compared to the values shown in Fig. 5a.

We have neglected the dependence on bulk composition of the thermophysical properties and radionuclide abundances that affect a planet's geodynamic evolution (Tables 1 and 2). More mafic compositions may lead to more vigorous convection and faster-cooling planets that may outgas comparatively more early on and less at later ages than the flux changes shown in Fig. 5a. The linkage between bulk compositions and radionuclide abundances is not straightforward. The internal distribution of radionuclides is unclear, because elements Th and U tend to be incorporated as impurities in minerals (Oelkers et al., 2009; Neveu et al., 2017) and because K can be exchanged between planet-building

materials such as silicates and volatile ices through aqueous alteration (Kirk & Stevenson, 1987; Engel et al., 1994; Castillo-Rogez & Lunine, 2010; Neveu et al., 2017). Moreover, the starting abundances of radionuclides are difficult to predict from first principles. The dominant heat source is ^{40}K, but Earth is rather depleted (relative to chondrites) in moderately volatile elements, including K, by unknown mechanisms (Desch et al., 2020; Unterborn et al., 2022). The solar system is probably not unusual in its abundances of short-lived radionuclides such as ^{26}Al, but these would be even more variable (Desch et al., 2022). Thus, radiogenic heating may best be left as a freely varied parameter, with the simulations shown here providing a solar system-centric baseline.

More mafic compositions tend to have a higher solidus temperature for a given pressure, and therefore are less prone to generating melt (i.e., outgassing). Although this was not tracked in our simulations, more mafic (reducing) compositions are generally expected to result in more reducing outgassing. The detailed carbon gas speciation into relative proportions of CO_2 and CH_4 depends on effects such as redox changes during ascent (Burgisser & Scaillet, 2007) and planet surface pressure (gravity and atmospheric density) (Gaillard & Scaillet, 2014), which are not considered here (Section 2.5).

Surface gravity is not expected to affect the continental weathering flux via the runoff rate to which this flux is proportional. Runoff rate is in turn proportional to river flow velocity, which depends on surface gravity as $v = 2gh$. Since declivity (a planet's relief) h is inversely proportional to surface gravity, the effects of gravity cancel out.

A planet's surface composition does affect the continental weathering flux to an extent comparable to the effect of residence time of rainwater on land (Fig. 6a). However, the effect of composition is much more pronounced on outgassing, for which it induces order-of-magnitude differences (Fig. 5a). Time-evolution simulations in which the atmospheric composition varies as a function of outgassing and (continental+seafloor) weathering show that in practice, the combined weathering flux varies to match the outgassing forcing so as to keep the sum of atmospheric and ocean carbon roughly constant within a factor of a few. An example such simulation, in which it is assumed that seafloor weathering proceeds as described in Section 2.3, is shown in Fig. 7. A broader set of such simulations for different planet sizes and compositions is presented in the companion paper.

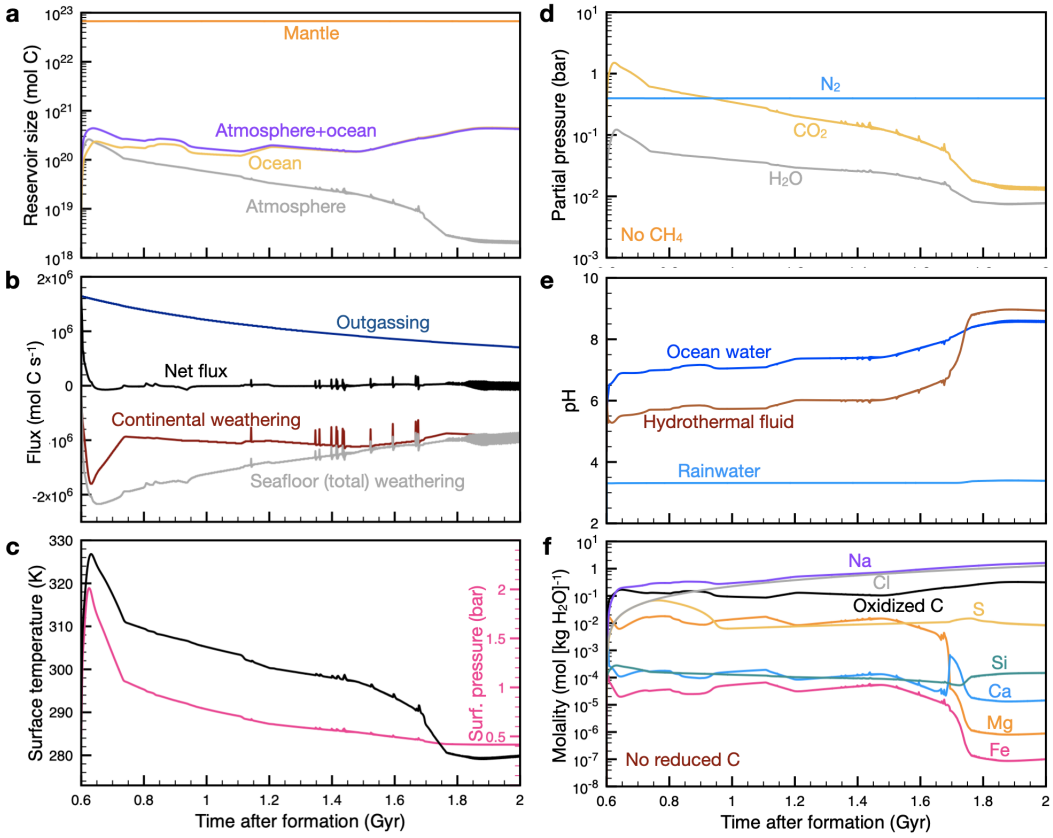

Figure 7. Time evolution of **a.** carbon reservoirs, **b.** carbon fluxes, **c.** surface temperature and pressure, **d.** atmospheric composition, **e.** pH, and **f.** ocean composition on a 1-$M_\oplus$ planet with an upper mantle composition comparable to that of mid-ocean ridge basalts (Table 4) and a surface composition comparable to that of Archean Earth (Table 5). The combined (continental + seafloor) weathering flux varies to match the outgassing forcing, maintaining roughly constant amounts of carbon in the {atmosphere+ocean} reservoir. Changes in the partitioning of carbon between the atmosphere and ocean arise due to secular changes in ocean chemistry (in this case, increasing pH). The ocean composition is initiated to the present-day composition, and the atmospheric composition is initiated to 0.5 bar total pressure of 80% N_2-20% CO_2.

Overall, planet mass and composition are expected to affect the carbon cycle as follows, assuming the planet receives insolation similar to Earth's. First, the magnitude of injection rates (fluxes) of carbon into the {atmosphere+ocean} reservoir varies by orders of magnitude (Fig. 5a) and is expected to generally decrease with geologic time. The added carbon, dissolved in rainwater and in the ocean, reacts with land and seafloor rock. The former yields an influx of carbon and cations into the ocean at a rate that is not very sensitive to surface composition or residence time (continental patchiness) (Fig. 6) and insensitive to planet mass (surface gravity), but which is proportional to rainfall rate (itself weakly increasing with temperature via the atmospheric H_2O content; Section 2.4) and land area. Continental patchiness affects evaporation, i.e., water:rock ratio, but simulations with water:rock ratios varied by a factor of a few do not yield major differences in weathering fluxes, especially since the effects of water:rock ratio and residence time offset each other (reactions with more concentrated reactants proceed faster). The finite solubility of carbon minerals drives precipitation and incorporation of carbon into the seafloor at rates that should match the rate of outgassing (Fig. 7). Variations in the continental weathering input of cations should drive changes in ocean composition on geological timescales that may affect the partitioning of carbon between the ocean and atmosphere due to the dependence of carbon speciation on, e.g., pH. Detailed investigation of these effects is the topic of the companion paper.

4.2 The Earth through time

While Earth's mean surface temperature has likely remained relatively constant at a few degrees above freezing throughout much of its evolution due to the carbonate-silicate cycle (Sleep & Zahnle, 2001), its land composition has become more felsic, its land less patchy, and its land coverage has increased (Korenaga, 2018). Its atmosphere has become less carbon-rich, with pCO_2 changing from about 0.1–1 bar to a few 10^{-4} bar (Catling & Zahnle, 2020).

This change in surface composition has acted to decrease continental weathering fluxes (Fig. 8) due to the lesser disequilibrium with Earth's atmosphere. Had Earth's composition remained the same, the continental weathering flux today would be closer to 100 Tmol yr^{-1} of carbon than the estimated 20–25 Tmol yr^{-1} (see Fig. 3c). However, the higher patchiness and lower areal fraction of land on Archean Earth implies a lower flux: about $55 \times \frac{L}{0.29}$ Tmol/year for a residence time of 0.1 rather than 10 years.

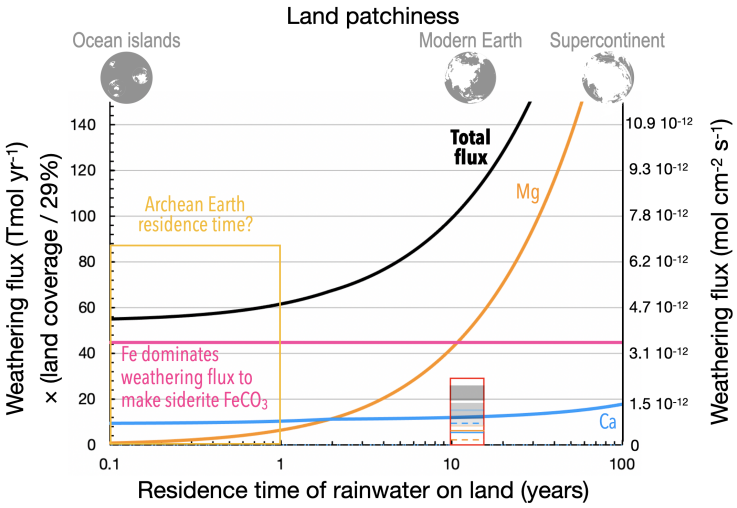

Figure 8. Effect of land coverage and patchiness on continental weathering flux for a 1-$M_\oplus$ planet. Here, we have assumed a primitive mantle composition for the Earth's crust, which may be adequate for the Archean, and an Archean-like atmospheric composition of 0.5 bar N_2 and 0.5 bar CO_2. The inset near 10 years residence time shows the same fluxes for modern Earth, as reproduced from Fig. 3.

This matches the modern-day weathering flux for a land fraction of about 15%, implying that the continental weathering flux need not have changed significantly over time.

The outgassing flux was likely an order of magnitude higher than today (Fig. 5a; see also Sleep and Zahnle (2001) and Krissansen-Totton, Arney, and Catling (2018)), implying a greater forcing that decreased with time. This flux was balanced by a greater seafloor weathering flux arising from a combination of higher convective velocity (Laneuville et al., 2018) and 3-5 times greater ridge length (Kadko et al., 1995) in equation (12) (lower water:rock ratio), even though, given the above, the accumulation rate of reactants from river delivery to the ocean was roughly the same as today. The gradual increase with time in the water:rock ratio of seafloor reactions, decrease in outgassing forcing, and negative feedback of the cycle likely all acted to maintain carbon levels in the atmosphere until carbon became significantly sequestered in biomass.

5 Conclusions

We have introduced a new, open-access model of geological carbon fluxes, whose implementation leverages existing, widely used geochemical codes of solid-melt equilib-

ria for silicate rocks (*MELTS*) and of equilibria and kinetics of water-rock interactions (*PHREEQC*). Coupled with a simple numerical computation of global thermal evolution, this model enables investigation of the effects of planet size (mass) and composition on carbon cycling through geologic time. Its applicable size range (0.5 to 2 Earth masses) is limited by the fidelity of the geodynamic model; the applicable range of composition is limited by those that can be handled by *MELTS* and *PHREEQC*.

We find that these planetary properties can influence outgassing fluxes of carbon by as much as two orders of magnitude, with 0.5–1-$M_\oplus$ planets with felsic upper mantles outgassing the most. In contrast, continental weathering fluxes are independent of planet size and relatively insensitive to surface composition in terms of disequilibrium with an Earth-like atmosphere; the variation in fluxes is at most a factor of a few. Continental patchiness (residence time of rainwater) has an effect of similar magnitude, with greater residence times generally leading to higher fluxes by allowing kinetically limited reactions to proceed further. Surface composition and land patchiness thus likely have lesser effects on continental weathering than the fraction of a planet's surface covered by land. These continental weathering fluxes likely affect the rate of change of oceanic chemical composition, which governs the partitioning of carbon between ocean and atmosphere. The resulting evolutions of atmosphere and ocean compositions on Earth-like planets of various sizes and solid compositions are the focus of a companion paper.

Open Research Section

The data supporting this paper's conclusions can be obtained by running the *ExoCcycleGeo* code (version 22.4) with the crust and upper mantle composition templates freely available from https://github.com/MarcNeveu/ExoCcycleGeo. The software dependencies can be downloaded at the following webpages:

PHREEQC: https://wwwbrr.cr.usgs.gov/projects/GWC_coupled/phreeqc;

alphaMELTS: https://magmasource.caltech.edu/alphamelts; *MELTS* itself is available at https://melts.ofm-research.org.

The data underlying Fig. 3 to 8 are archived in a Zenodo repository at https://zenodo.org/deposit/7640681 (size: 377.5 MBytes). The subset of data underlying Fig. 3, 4, 6, and 8 were obtained by running *PHREEQC* alone. Those underlying Fig. 2 were obtained by hard-coding a value for the mid-mantle temperature in *ExoCcycleGeo* and running a single time step.

Acknowledgments

This work was funded by NASA Exoplanet Research Program award NNX17AB95G. We thank the reviewers of the proposal that led to this award for providing valuable feedback and guidance that helped improve this research.

References

Abbot, D. S., Cowan, N. B., & Ciesla, F. J. (2012). Indication of insensitivity of planetary weathering behavior and habitable zone to surface land fraction. *The Astrophysical Journal*, *756*(2), 178. doi: 10.1088/0004-637X/756/2/178

Akaogi, M., & Ito, E. (1993). Heat capacity of $MgSiO_3$ perovskite. *Geophysical Research Letters*, *20*(2), 105–108. doi: 10.1029/92GL02655

Akeson, R., Chen, X., Ciardi, D., Crane, M., Good, J., Harbut, M., ... Zhang, A. (2013). The NASA Exoplanet Archive: data and tools for exoplanet research. *Publications of the Astronomical Society of the Pacific*, *125*(930), 989. doi: 10.1086/672273

Allan, J. F., Batiza, R., Perfit, M. R., Fornari, D. J., & Sack, R. O. (1989). Petrology of lavas from the lamont seamount chain and adjacent East Pacific Rise, 10 N. *Journal of Petrology*, *30*(5), 1245–1298. doi: 10.1093/petrology/30.5.1245

Allen, M. R., & Ingram, W. J. (2002). Constraints on future changes in climate and the hydrologic cycle. *Nature*, *419*(6903), 228–232.

Anderson, A. (1995). CO_2 and the eruptibility of picrite and komatiite. *Lithos*, *34*(1-3), 19–25. doi: 10.1016/0024-4937(95)90005-5

Anderson, G. M. (2005). *Thermodynamics of Natural Systems*. Cambridge University Press.

Anderson, W. W., & Ahrens, T. J. (1994). An equation of state for liquid iron and implications for the Earth's core. *Journal of Geophysical Research: Solid Earth*, *99*(B3), 4273–4284. doi: 10.1029/93JB03158

Antoshechkina, P., & Asimow, P. (2018). *Alphamelts software manual – a text driven interface for MELTS, pMELTS & pHMELTS* (Tech. Rep.). California Institute of Technology.

Antoshechkina, P. M., & Asimow, P. D. (2010). Adiabat_1ph 3.0 and the MAGMA website: educational and research tools for studying the petrology and geo-

chemistry of plate margins. In *AGU Fall Meeting Abstracts* (Vol. 2010, pp. ED41B–0644).

Antoshechkina, P. M., Asimow, P. D., Hauri, E. H., & Luffi, P. I. (2010). Effect of water on mantle melting and magma differentiation, as modeled using Adiabat_1ph 3.0. In *AGU Fall Meeting Abstracts* (Vol. 2010, pp. V53C–2264).

Arney, G. N., Domagal-Goldman, S. D., Meadows, V. S., Wolf, E. T., Schwieterman, E., Charnay, B., ... Trainer, M. G. (2016). The pale orange dot: the spectrum and habitability of hazy Archean Earth. *Astrobiology*, *16*(11), 873–899. doi: 10.1089/ast.2015.1422

Arney, G. N., Meadows, V. S., Domagal-Goldman, S. D., Deming, D., Robinson, T. D., Tovar, G., ... Schwieterman, E. (2017). Pale orange dots: the impact of organic haze on the habitability and detectability of Earthlike exoplanets. *The Astrophysical Journal*, *836*(1), 49. doi: 10.3847/1538-4357/836/1/49

Asimow, P. D., & Ghiorso, M. S. (1998). Algorithmic modifications extending MELTS to calculate subsolidus phase relations. *American Mineralogist*, *83*(9-10), 1127–1132. doi: 10.2138/am-1998-9-1022

Auzende, A.-L., Pellenq, R.-M., Devouard, B., Baronnet, A., & Grauby, O. (2006). Atomistic calculations of structural and elastic properties of serpentine minerals: the case of lizardite. *Physics and Chemistry of Minerals*, *33*(4), 266–275. doi: 10.1007/s00269-006-0078-x

Barnes, R., Luger, R., Deitrick, R., Driscoll, P., Quinn, T. R., Fleming, D. P., ... Armstrong, J. (2020). VPLanet: the virtual planet simulator. *Publications of the Astronomical Society of the Pacific*, *132*(1008), 024502. doi: 10.1088/1538-3873/ab3ce8

Barnes, R., Meadows, V. S., & Evans, N. (2015). Comparative habitability of transiting exoplanets. *The Astrophysical Journal*, *814*(2), 91. doi: 10.1088/0004-637X/814/2/91

Barnes, R., Mullins, K., Goldblatt, C., Meadows, V. S., Kasting, J. F., & Heller, R. (2013). Tidal Venuses: triggering a climate catastrophe via tidal heating. *Astrobiology*, *13*(3), 225–250. doi: 10.1089/ast.2012.0851

Begemann, F., & Libby, W. F. (1957). Continental water balance, ground water inventory and storage times, surface ocean mixing rates and world-wide water circulation patterns from cosmic-ray and bomb tritium. *Geochimica et*

Cosmochimica Acta, *12*(4), 277–296. doi: 10.1016/0016-7037(57)90040-6

Berner, R. A., Lasaga, A. C., & Garrels, R. M. (1983). The carbonate-silicate geochemical cycle and its effect on atmospheric carbon dioxide over the past 100 million years. *American Journal of Science*, *283*, 641–683. doi: 10.2475/ajs.283.7.641

Bhatia, G. K., & Sahijpal, S. (2016). The early thermal evolution of Mars. *Meteoritics and Planetary Science*, *51*(1), 138-154. doi: 10.1111/maps.12573

Bhatia, G. K., & Sahijpal, S. (2017). Did ^{26}Al and impact-induced heating differentiate Mercury? *Meteoritics and Planetary Science*, *52*(2), 295-319. doi: 10.1111/maps.12789

Blackledge, B., Green, J., Barnes, R., & Way, M. J. (2020). Tides on other Earths: Implications for exoplanet and palaeo-tidal simulations. *Geophysical Research Letters*, *47*(12), e2019GL085746. doi: https://doi.org/10.1029/2019GL085746

Blundy, J., Cashman, K. V., Rust, A., & Witham, F. (2010). A case for CO_2-rich arc magmas. *Earth and Planetary Science Letters*, *290*(3-4), 289–301. doi: 10.1016/j.epsl.2009.12.013

Bond, J. C., O'Brien, D. P., & Lauretta, D. S. (2010). The compositional diversity of extrasolar terrestrial planets. I. In situ simulations. *The Astrophysical Journal*, *715*(2), 1050. doi: 10.1088/0004-637X/715/2/1050

Broecker, W. S., & Peng, T. H. (1982). *Tracers in the Sea*. Lamont-Doherty Geological Observatory, Palisades, NY.

Brown, M., Johnson, T., & Gardiner, N. J. (2020). Plate tectonics and the archean earth. *Annual Review of Earth and Planetary Sciences*, *48*, 291–320. doi: 10.1146/annurev-earth-081619-052705

Burgisser, A., & Scaillet, B. (2007). Redox evolution of a degassing magma rising to the surface. *Nature*, *445*(7124), 194–197. doi: 10.1038/nature05509

Burton, M. R., Sawyer, G. M., & Granieri, D. (2013). Deep carbon emissions from volcanoes. *Reviews in Mineralogy and Geochemistry*, *75*(1), 323–354. doi: 10.2138/rmg.2013.75.11

Byerlee, J. (1978). Friction of rocks. In *Rock Friction and Earthquake Prediction* (pp. 615–626). Springer.

Caldeira, K., & Kasting, J. F. (1992). The life span of the biosphere revisited. *Nature*, *360*(6406), 721–723. doi: 10.1038/360721a0

Canup, R. M. (2004). Simulations of a late lunar-forming impact. *Icarus*, *168*(2), 433–456. doi: 10.1016/j.icarus.2003.09.028

Canup, R. M., Kratter, K. M., & Neveu, M. (2021). On the origin of the Pluto system. In *The Pluto System after New Horizons* (p. 475-506). University of Arizona Press.

Castillo-Rogez, J. C., & Lunine, J. I. (2010). Evolution of Titan's rocky core constrained by Cassini observations. *Geophysical Research Letters*, *37*(20). doi: 10.1029/2010GL044398

Catling, D. C., Kiang, N. Y., Robinson, T. D., Rushby, A. J., Del Genio, A., et al. (2018). Exoplanet biosignatures: a framework for their assessment. *Astrobiology*. doi: 10.1089/ast.2017.1737

Catling, D. C., & Zahnle, K. J. (2020). The Archean atmosphere. *Science Advances*, *6*(9), eaax1420. doi: 10.1126/sciadv.aax1420

Chahine, M. T. (1992). The hydrological cycle and its influence on climate. *Nature*, *359*(6394), 373–380. doi: 10.1038/359373a0

Choukroun, M., & Grasset, O. (2010). Thermodynamic data and modeling of the water and ammonia-water phase diagrams up to 2.2 GPa for planetary geophysics. *The Journal of Chemical Physics*, *133*(14), 144502. doi: 10.1063/1.3487520

Chung, D. (1971). Elasticity and equations of state of olivines in the Mg_2SiO_4-Fe_2SiO_4 system. *Geophysical Journal International*, *25*(5), 511–538. doi: 10.1111/j.1365-246X.1971.tb02201.x

Cioni, R. (2000). Volatile content and degassing processes in the AD 79 magma chamber at Vesuvius (Italy). *Contributions to Mineralogy and Petrology*, *140*(1), 40–54. doi: 10.1007/s004100000167

Cogné, J.-P., & Humler, E. (2006). Trends and rhythms in global seafloor generation rate. *Geochemistry, Geophysics, Geosystems*, *7*(3). doi: 10.1029/2005GC001148

Cohen, S. D., Hindmarsh, A. C., & Dubois, P. F. (1996). CVODE, a stiff/nonstiff ODE solver in C. *Computers in Physics*, *10*(2), 138–143. doi: 10.1063/1.4822377

Colbourn, G., Ridgwell, A., & Lenton, T. (2015). The time scale of the silicate weathering negative feedback on atmospheric CO_2. *Global Biogeochemical Cy-*

cles, *29*(5), 583–596. doi: 10.1002/2014GB005054

Cole, J. J., & Caraco, N. F. (2001). Carbon in catchments: connecting terrestrial carbon losses with aquatic metabolism. *Marine and Freshwater Research*, *52*(1), 101–110. doi: 10.1071/MF00084

Colose, C. M., Haqq-Misra, J., Wolf, E. T., Del Genio, A. D., Barnes, R., Way, M. J., & Ruedy, R. (2021). Effects of spin–orbit resonances and tidal heating on the inner edge of the habitable zone. *The Astrophysical Journal*, *921*(1), 25. doi: 10.3847/1538-4357/ac135c

Dasgupta, R., & Hirschmann, M. M. (2010). The deep carbon cycle and melting in Earth's interior. *Earth and Planetary Science Letters*, *298*(1-2), 1–13. doi: 10.1016/j.epsl.2010.06.039

De Sanctis, M. C., Ammannito, E., Raponi, A., Marchi, S., McCord, T. B., McSween, H., ... Russell, C. T. (2015). Ammoniated phyllosilicates with a likely outer solar system origin on (1) Ceres. *Nature*, *528*(7581), 241–244. doi: 10.1038/nature16172

Desch, S. J., Abbot, D., Krijt, S., Unterborn, C., Morard, G., & Hartnett, H. E. (2020). The volatile content of rocky planets. In *Planetary Diversity: Rocky planet processes and their observational signatures* (pp. 6.1–6.40). IOP.

Desch, S. J., Young, E. D., Dunham, E. T., Fujimoto, Y., & Dunlap, D. R. (2022). Short-Lived Radionuclides in Meteorites and the Sun's Birth Environment. *arXiv e-prints*. doi: 10.48550/arXiv.2203.11169

Deschamps, F., & Sotin, C. (2000). Inversion of two-dimensional numerical convection experiments for a fluid with a strongly temperature-dependent viscosity. *Geophysical Journal International*, *143*(1), 204–218. doi: 10.1046/j.1365-246x.2000.00228.x

Des Marais, D. J., Jakosky, B. M., & Hynek, B. M. (2007). Astrobiological implications of Mars' surface composition and properties. In *The Martian Surface–Composition, Mineralogy, and Physical Properties* (pp. 599–624). Cambridge University Press.

Dolinschi, J. D. (2019). Mineralogy of the silicon-rich mantle: Implications for Mars and exoplanets. *PhD dissertation*. Retrieved from `https://keep.lib.asu.edu/_flysystem/fedora/c7/218100/Dolinschi_asu_0010N_19331.pdf`

Domagal-Goldman, S. D., Segura, A., Claire, M. W., Robinson, T. D., & Meadows,

V. S. (2014). Abiotic ozone and oxygen in atmospheres similar to prebiotic Earth. *The Astrophysical Journal*, *792*(2), 90. doi: 10.1088/0004-637X/792/2/90

Donnadieu, Y., Goddéris, Y., Pierrehumbert, R., Dromart, G., Fluteau, F., & Jacob, R. (2006). A GEOCLIM simulation of climatic and biogeochemical consequences of Pangea breakup. *Geochemistry, Geophysics, Geosystems*, *7*(11). doi: 10.1029/2006GC001278

Dressing, C. D., Spiegel, D. S., Scharf, C. A., Menou, K., & Raymond, S. N. (2010). Habitable climates: the influence of eccentricity. *The Astrophysical Journal*, *721*(2), 1295. doi: 10.1088/0004-637X/721/2/1295

Dubrovinsky, L. S., Saxena, S. K., Tutti, F., Rekhi, S., & LeBehan, T. (2000). In situ X-ray study of thermal expansion and phase transition of iron at multimegabar pressure. *Physical Review Letters*, *84*(8), 1720. doi: 10.1103/PhysRevLett.84.1720

Duffy, T. S., Hemley, R. J., & Mao, H.-K. (1995). Equation of state and shear strength at multimegabar pressures: Magnesium oxide to 227 GPa. *Physical Review Letters*, *74*(8), 1371. doi: 10.1103/PhysRevLett.74.1371

Duffy, T. S., Meade, C., Fei, Y., Mao, H.-K., & Hemley, R. J. (1995). High-pressure phase transition in brucite, Mg $(OH)_2$. *American Mineralogist*, *80*(3-4), 222–230. doi: 10.2138/am-1995-3-403

Dyar, M. D., Helbert, J., Cooper, R. F., Sklute, E. C., Maturilli, A., Mueller, N. T., ... Smrekar, S. E. (2021). Surface weathering on Venus: Constraints from kinetic, spectroscopic, and geochemical data. *Icarus*, *358*, 114139. doi: 10.1016/j.icarus.2020.114139

Edson, A. R., Kasting, J. F., Pollard, D., Lee, S., & Bannon, P. R. (2012). The carbonate-silicate cycle and CO_2/climate feedbacks on tidally locked terrestrial planets. *Astrobiology*, *12*(6), 562–571. doi: 10.1089/ast.2011.0762

Engel, S., Lunine, J. I., & Norton, D. L. (1994). Silicate interactions with ammonia-water fluids on early Titan. *Journal of Geophysical Research: Planets*, *99*(E2), 3745–3752. doi: 10.1029/93JE03433

Fei, Y., Prewitt, C. T., Mao, H.-k., & Bertka, C. M. (1995). Structure and density of FeS at high pressure and high temperature and the internal structure of Mars. *Science*, *268*(5219), 1892–1894. doi: 10.1126/science.268.5219.1892

Felton, R. C., Bastelberger, S. T., Mandt, K. E., Luspay-Kuti, A., Fauchez, T. J., & Domagal-Goldman, S. D. (2022). The role of atmospheric exchange in false-positive biosignature detection. *Journal of Geophysical Research: Planets*, *127*(3), e2021JE006853. doi: 10.1029/2021JE006853

Fischer, K. M., Ford, H. A., Abt, D. L., & Rychert, C. A. (2010). The lithosphere-asthenosphere boundary. *Annual Review of Earth and Planetary Sciences*, *38*, 551–575. doi: 10.1146/annurev-earth-040809-152438

Foley, B. J. (2015). The role of plate tectonic–climate coupling and exposed land area in the development of habitable climates on rocky planets. *The Astrophysical Journal*, *812*(1), 36. doi: 10.1088/0004-637X/812/1/36

Forget, F., & Leconte, J. (2014). Possible climates on terrestrial exoplanets. *Phil. Trans. R. Soc. A*, *372*(2014), 20130084. doi: 10.1098/rsta.2013.0084

Fortes, A. D., Brand, H., Vočadlo, L., Lindsay-Scott, A., Fernandez-Alonso, F., & Wood, I. (2013). P–V–T equation of state of synthetic mirabilite ($Na_2SO_4{\cdot}10D_2O$) determined by powder neutron diffraction. *Journal of Applied Crystallography*, *46*(2), 448–460. doi: 10.1107/S0021889813001362

Fortes, A. D., Wood, I. G., Brodholt, J. P., & Vočadlo, L. (2003). The structure, ordering and equation of state of ammonia dihydrate ($NH_3{\cdot}2H_2O$). *Icarus*, *162*(1), 59–73. doi: 10.1016/S0019-1035(02)00073-8

Frank, M. R., Aarestad, E., Scott, H. P., & Prakapenka, V. B. (2013). A comparison of ice VII formed in the H_2O, NaCl–H_2O, and CH_3OH–H_2O systems: Implications for H_2O-rich planets. *Physics of the Earth and Planetary Interiors*, *215*, 12–20. doi: 10.1016/j.pepi.2012.10.010

Fujii, Y., Angerhausen, D., Deitrick, R., Domagal-Goldman, S., Grenfell, J. L., Hori, Y., ... Stevenson, K. B. (2018). Exoplanet biosignatures: observational prospects. *Astrobiology*, *18*(6), 739–778. doi: 10.1089/ast.2017.1733

Gaillard, F., & Scaillet, B. (2014). A theoretical framework for volcanic degassing chemistry in a comparative planetology perspective and implications for planetary atmospheres. *Earth and Planetary Science Letters*, *403*, 307–316. doi: 10.1016/j.epsl.2014.07.009

Gaillard, F., Scaillet, B., & Arndt, N. T. (2011). Atmospheric oxygenation caused by a change in volcanic degassing pressure. *Nature*, *478*(7368), 229. doi: 10.1038/nature10460

Gerlach, T. M., & Graeber, E. J. (1985). Volatile budget of Kilauea volcano. *Nature*, *313*(6000), 273–277. doi: 10.1038/313273a0

Ghiorso, M. S., & Sack, R. O. (1995). Chemical mass transfer in magmatic processes IV. A revised and internally consistent thermodynamic model for the interpolation and extrapolation of liquid-solid equilibria in magmatic systems at elevated temperatures and pressures. *Contributions to Mineralogy and Petrology*, *119*(2), 197–212. doi: 10.1007/BF00307281

Gibbs, R. (1975). *Assessing Potential Ocean Pollutants*. National Academy of Sciences.

Gillon, M., Triaud, A. H., Demory, B.-O., Jehin, E., Agol, E., Deck, K. M., ... Queloz, D. (2017). Seven temperate terrestrial planets around the nearby ultracool dwarf star TRAPPIST-1. *Nature*, *542*(7642), 456–460. doi: 10.1038/nature21360

Grenfell, J. L. (2017). A review of exoplanetary biosignatures. *Physics Reports*, *713*, 1–17. doi: 10.1016/j.physrep.2017.08.003

Griffiths, G. I., Fortes, A. D., Pickard, C. J., & Needs, R. (2012). Crystal structure of ammonia dihydrate II. *The Journal of Chemical Physics*, *136*(17), 174512. doi: 10.1063/1.4707930

Gromnitskaya, E. L., Yagafarov, O. F., Lyapin, A. G., Brazhkin, V. V., Wood, I. G., Tucker, M. G., & Fortes, A. D. (2013). The high-pressure phase diagram of synthetic epsomite ($MgSO_4{\cdot}7H_2O$ and $MgSO_4{\cdot}7D_2O$) from ultrasonic and neutron powder diffraction measurements. *Physics and Chemistry of Minerals*, *40*(3), 271–285. doi: 10.1007/s00269-013-0567-7

Haqq-Misra, J. D., Domagal-Goldman, S. D., Kasting, P. J., & Kasting, J. F. (2008). A revised, hazy methane greenhouse for the Archean Earth. *Astrobiology*, *8*(6), 1127–1137. doi: 10.1089/ast.2007.0197

Harrison, C. (1999). Constraints on ocean volume change since the Archean. *Geophysical Research Letters*, *26*(13), 1913–1916. doi: 10.1029/1999GL900425

Hartley, M. E., Maclennan, J., Edmonds, M., & Thordarson, T. (2014). Reconstructing the deep CO_2 degassing behaviour of large basaltic fissure eruptions. *Earth and Planetary Science Letters*, *393*, 120–131. doi: 10.1016/j.epsl.2014.02.031

Hasenclever, J., Theissen-Krah, S., Rüpke, L. H., Morgan, J. P., Iyer, K., Petersen, S., & Devey, C. W. (2014). Hybrid shallow on-axis and deep off-axis hy-

drothermal circulation at fast-spreading ridges. *Nature*, *508*(7497), 508–512. doi: 10.1038/nature13174

Hekinian, R., Pineau, F., Shilobreeva, S., Bideau, D., Gracia, E., & Javoy, M. (2000). Deep sea explosive activity on the Mid-Atlantic Ridge near 34 50' N: magma composition, vesicularity and volatile content. *Journal of Volcanology and Geothermal Research*, *98*(1-4), 49–77. doi: 10.1016/S0377-0273(99)00190-0

Hofmann, A. W. (1988). Chemical differentiation of the Earth: the relationship between mantle, continental crust, and oceanic crust. *Earth and Planetary Science Letters*, *90*(3), 297–314. doi: 10.1016/0012-821X(88)90132-X

Hu, R., Seager, S., & Bains, W. (2012). Photochemistry in terrestrial exoplanet atmospheres. I. Photochemistry model and benchmark cases. *The Astrophysical Journal*, *761*(2), 166. doi: 10.1088/0004-637X/761/2/166

Johansen, A., Ronnet, T., Bizzarro, M., Schiller, M., Lambrechts, M., Nordlund, Å., & Lammer, H. (2021). A pebble accretion model for the formation of the terrestrial planets in the Solar System. *Science Advances*, *7*(8), eabc0444. doi: 10.1126/sciadv.abc0444

Johnson, H. P., & Pruis, M. J. (2003). Fluxes of fluid and heat from the oceanic crustal reservoir. *Earth and Planetary Science Letters*, *216*(4), 565–574. doi: 10.1016/S0012-821X(03)00545-4

Jones, M., Soule, S., Gonnermann, H., Le Roux, V., & Clague, D. (2018). Magma ascent and lava flow emplacement rates during the 2011 Axial Seamount eruption based on CO_2 degassing. *Earth and Planetary Science Letters*, *494*, 32–41. doi: 10.1016/j.epsl.2018.04.044

Kadko, D., Baross, J., & Alt, J. (1995). The magnitude and global implications of hydrothermal flux. *Geophysical Monograph-American Geophysical Union*, *91*, 446–466. doi: 10.1029/GM091p0446

Kane, S. R., Hill, M. L., Kasting, J. F., Kopparapu, R. K., Quintana, E. V., Barclay, T., ... Torres, G. (2016). A catalog of Kepler habitable zone exoplanet candidates. *The Astrophysical Journal*, *830*(1), 1. doi: 10.3847/0004-637X/830/1/1

Kaspi, Y., & Showman, A. P. (2015). Atmospheric dynamics of terrestrial exoplanets over a wide range of orbital and atmospheric parameters. *The Astrophysical*

Journal, *804*(1), 60. doi: 10.1088/0004-637X/804/1/60

Kasting, J. F. (1988). Runaway and moist greenhouse atmospheres and the evolution of Earth and Venus. *Icarus*, *74*(3), 472–494. doi: 10.1016/0019-1035(88)90116-9

Kasting, J. F., & Ackerman, T. P. (1986). Climatic consequences of very high carbon dioxide levels in the Earth's early atmosphere. *Science*, *234*(4782), 1383–1385. doi: 10.1126/science.11539665

Katsura, T., Yoneda, A., Yamazaki, D., Yoshino, T., & Ito, E. (2010). Adiabatic temperature profile in the mantle. *Physics of the Earth and Planetary Interiors*, *183*(1-2), 212–218. doi: 10.1016/j.pepi.2010.07.001

Kiang, N. Y., Domagal-Goldman, S., Parenteau, M. N., Catling, D. C., Fujii, Y., Meadows, V. S., ... Walker, S. I. (2018). Exoplanet biosignatures: at the dawn of a new era of planetary observations. *Astrobiology*, *18*(6), 619–629. doi: 10.1089/ast.2018.1862

Kiessling, W., Flügel, E., & Golonka, J. (2003). Patterns of Phanerozoic carbonate platform sedimentation. *Lethaia*, *36*(3), 195–225. doi: 10.1080/00241160310004648

Kirk, R. L., & Stevenson, D. J. (1987). Thermal evolution of a differentiated Ganymede and implications for surface features. *Icarus*, *69*(1), 91–134. doi: 10.1016/0019-1035(87)90009-1

Kite, E. S., Manga, M., & Gaidos, E. (2009). Geodynamics and rate of volcanism on massive Earth-like planets. *The Astrophysical Journal*, *700*(2), 1732. doi: 10.1088/0004-637X/700/2/1732

Kopparapu, R. K., Ramirez, R., Kasting, J. F., Eymet, V., Robinson, T. D., Mahadevan, S., ... Deshpande, R. (2013). Habitable zones around main-sequence stars: New estimates. *The Astrophysical Journal*, *765*, 131. doi: 10.1088/0004-637X/765/2/131

Kopparapu, R. K., Wolf, E. T., & Meadows, V. S. (2020). Characterizing exoplanet habitability. In *Planetary Astrobiology* (p. 449). University of Arizona Press.

Korenaga, J. (2008). Urey ratio and the structure and evolution of Earth's mantle. *Reviews of Geophysics*, *46*(2). doi: 10.1029/2007RG000241

Korenaga, J. (2018). Crustal evolution and mantle dynamics through Earth history. *Philosophical Transactions of the Royal Society A: Mathematical, Physical and*

Engineering Sciences, *376*(2132), 20170408. doi: 10.1098/rsta.2017.0408

Korenaga, J., & Karato, S.-I. (2008). A new analysis of experimental data on olivine rheology. *Journal of Geophysical Research: Solid Earth*, *113*(B2). doi: 10.1029/2007JB005100

Krissansen-Totton, J., Arney, G. N., & Catling, D. C. (2018). Constraining the climate and ocean pH of the early Earth with a geological carbon cycle model. *Proceedings of the National Academy of Sciences*, *115*(16), 4105–4110. doi: 10.1073/pnas.1721296115

Krissansen-Totton, J., Bergsman, D. S., & Catling, D. C. (2016). On detecting biospheres from chemical thermodynamic disequilibrium in planetary atmospheres. *Astrobiology*, *16*(1), 39–67. doi: 10.1089/ast.2015.1327

Krissansen-Totton, J., & Catling, D. C. (2017). Constraining climate sensitivity and continental versus seafloor weathering using an inverse geological carbon cycle model. *Nature Communications*, *8*(1), 1–15. doi: 10.1038/ncomms15423

Krissansen-Totton, J., Garland, R., Irwin, P., & Catling, D. C. (2018). Detectability of biosignatures in anoxic atmospheres with the James Webb Space Telescope: A TRAPPIST-1e case study. *The Astronomical Journal*, *156*(3), 114. doi: 10.3847/1538-3881/aad564

Krissansen-Totton, J., Thompson, M., Galloway, M. L., & Fortney, J. J. (2022). Understanding planetary context to enable life detection on exoplanets and test the Copernican principle. *Nature Astronomy*, *6*(2), 189–198. doi: 10.1038/s41550-021-01579-7

Laneuville, M., Kameya, M., & Cleaves, H. J. (2018). Earth without life: A systems model of a global abiotic nitrogen cycle. *Astrobiology*, *18*, 897–914. doi: 10.1089/ast.2017.1700

Lehmer, O. R., Catling, D. C., & Krissansen-Totton, J. (2020). Carbonate-silicate cycle predictions of Earth-like planetary climates and testing the habitable zone concept. *Nature Communications*, *11*(1), 1–10. doi: 10.1038/s41467-020-19896-2

Lerman, A., & Wu, L. (2006). CO_2 and sulfuric acid controls of weathering and river water composition. *Journal of Geochemical Exploration*, *88*(1-3), 427–430. doi: 10.1016/j.gexplo.2005.08.100

Lerman, A., Wu, L., & Mackenzie, F. T. (2007). CO_2 and H_2SO_4 consump-

tion in weathering and material transport to the ocean, and their role in the global carbon balance. *Marine Chemistry*, *106*(1-2), 326–350. doi: 10.1016/j.marchem.2006.04.004

Lewis, N. T., Lambert, F. H., Boutle, I. A., Mayne, N. J., Manners, J., & Acreman, D. M. (2018). The influence of a substellar continent on the climate of a tidally locked exoplanet. *The Astrophysical Journal*, *854*(2), 171.

Lin, Z., MacDonald, R. J., Kaltenegger, L., & Wilson, D. J. (2021). Differentiating modern and prebiotic Earth scenarios for TRAPPIST-1e: high-resolution transmission spectra and predictions for JWST. *Monthly Notices of the Royal Astronomical Society*, *505*(3), 3562–3578. doi: 10.1093/mnras/stab1486

Lisse, C. M., Desch, S. J., Unterborn, C. T., Kane, S. R., Young, P. R., Hartnett, H. E., ... Izenberg, N. R. (2020). A geologically robust procedure for observing rocky exoplanets to ensure that detection of atmospheric oxygen is a modern Earth-like biosignature. *The Astrophysical Journal Letters*, *898*(1), L17. doi: 10.3847/2041-8213/ab9b91

Lorenzo, A., Desch, S. J., & Shim, S.-H. (2014). On the lower radius limit of exoplanets. In *Lunar and Planetary Science Conference* (p. 1636).

Lynch, J. K., Beatty, C. M., Seidel, M. P., Jungst, L. J., & DeGrandpre, M. D. (2010). Controls of riverine CO_2 over an annual cycle determined using direct, high temporal resolution pCO_2 measurements. *Journal of Geophysical Research: Biogeosciences*, *115*(G3). doi: 10.1029/2009JG001132

Lyubetskaya, T., & Korenaga, J. (2007). Chemical composition of Earth's primitive mantle and its variance: 1. Method and results. *Journal of Geophysical Research: Solid Earth*, *112*(B3). doi: 10.1029/2005JB004223

Ma, C., Wu, X., Huang, F., Zhou, Q., Li, F., & Cui, Q. (2012). The acoustic velocity, refractive index, and equation of state of liquid ammonia dihydrate under high pressure and high temperature. *The Journal of Chemical Physics*, *137*(10), 104504. doi: 10.1063/1.4751944

Madden, J., & Kaltenegger, L. (2020). How surfaces shape the climate of habitable exoplanets. *Monthly Notices of the Royal Astronomical Society*, *495*(1), 1–11. doi: 10.1093/mnras/staa387

Martin, J.-M., & Meybeck, M. (1979). Elemental mass-balance of material carried by major world rivers. *Marine Chemistry*, *7*(3), 173–206. doi: 10.1016/0304

-4203(79)90039-2

McDonough, W. F., & Sun, S.-S. (1995). The composition of the Earth. *Chemical Geology*, *120*(3-4), 223–253. doi: 10.1016/0009-2541(94)00140-4

McKenzie, D. A. N., & Bickle, M. J. (1988). The volume and composition of melt generated by extension of the lithosphere. *Journal of Petrology*, *29*(3), 625–679. doi: 10.1093/petrology/29.3.625

McLennan, S. M., & Grotzinger, J. P. (2008). The sedimentary rock cycle of Mars. In *The Martian Surface–Composition, Mineralogy, and Physical Properties* (pp. 541–577). Cambridge University Press.

Mikal-Evans, T. (2022). Detecting the proposed CH_4–CO_2 biosignature pair with the James Webb Space Telescope: TRAPPIST-1e and the effect of cloud/haze. *Monthly Notices of the Royal Astronomical Society*, *510*(1), 980–991. doi: 10.1093/mnras/stab3383

Ming, D. W., Morris, R. V., & Clark, B. C. (2008). Aqueous alteration on Mars. In *The Martian Surface–Composition, Mineralogy, and Physical Properties* (pp. 519–540). Cambridge University Press.

Moresi, L.-N., & Solomatov, V. S. (1995). Numerical investigation of 2D convection with extremely large viscosity variations. *Physics of Fluids*, *7*(9), 2154–2162. doi: 10.1063/1.868465

Mottl, M. J. (1983). Metabasalts, axial hot springs, and the structure of hydrothermal systems at mid-ocean ridges. *Geological Society of America Bulletin*, *94*(2), 161–180. doi: https://doi.org/10.1130/0016-7606(1983)94\%3C161:MAHSAT\%3E2.0.CO;2

Nesbitt, H. W., & Markovics, G. (1997). Weathering of granodioritic crust, long-term storage of elements in weathering profiles, and petrogenesis of siliciclastic sediments. *Geochimica et Cosmochimica Acta*, *61*(8), 1653–1670. doi: 10.1016/S0016-7037(97)00031-8

Nestola, F., Angel, R. J., Zhao, J., Garrido, C. J., Sánchez-Vizcaíno, V. L., Capitani, G., & Mellini, M. (2010). Antigorite equation of state and anomalous softening at 6 GPa: an in situ single-crystal x-ray diffraction study. *Contributions to Mineralogy and Petrology*, *160*(1), 33–43. doi: 10.1007/s00410-009-0463-9

Neveu, M., Desch, S. J., & Castillo-Rogez, J. C. (2017). Aqueous geochemistry in icy world interiors: Equilibrium fluid, rock, and gas compositions, and fate

of antifreezes and radionuclides. *Geochimica et Cosmochimica Acta*, *212*, 324–371. doi: 10.1016/j.gca.2017.06.023

Nordstrom, D. K., Plummer, L. N., Wigley, T. M. L., Wolery, T. J., Ball, J. W., Jenne, E. A., ... Thrailkill, J. (1979). A comparison of computerized chemical models for equilibrium calculations in aqueous systems. In *ACS Symposium Series* (Vol. 93, p. 857-892). ACS Publications. doi: 10.1021/bk-1979-0093.ch038

Oelkers, E., Bénézeth, P., & Pokrovski, G. S. (2009). Thermodynamic databases for water-rock interaction. *Reviews in Mineralogy and Geochemistry*, *70*(1), 1–46. doi: 10.2138/rmg.2009.70.1

Orgel, L. E. (1998). The origin of life–a review of facts and speculations. *Trends in Biochemical Sciences*, *23*(12), 491–495. doi: 10.1016/s0968-0004(98)01300-0

Palandri, J. L., & Kharaka, Y. K. (2004). *A compilation of rate parameters of water-mineral interaction kinetics for application to geochemical modeling* (Tech. Rep.). US Geological Survey. Menlo Park. CA.

Pamukcu, A. S., Gualda, G. A. R., Ghiorso, M. S., Miller, C. F., & McCracken, R. G. (2015). Phase-equilibrium geobarometers for silicic rocks based on rhyolite-MELTS—Part 3: Application to the Peach Spring tuff (Arizona–California–Nevada, USA). *Contributions to Mineralogy and Petrology*, *169*(3), 33. doi: 10.1007/s00410-015-1122-y

Papike, J. J., Ryder, G., & Shearer, C. K. (1998). Lunar samples. In J. J. Papike (Ed.), *Planetary Materials* (Vol. 36). Walter de Gruyter GmbH & Co KG.

Parkhurst, D. L., & Appelo, C. A. J. (2013). *Description of input and examples for PHREEQC version 3–A computer program for speciation, batch-reaction, one-dimensional transport, and inverse geochemical calculations* (Tech. Rep.). US Geological Survey, Reston, VA.

Pendergrass, A. G. (2020). The global-mean precipitation response to CO_2-induced warming in CMIP6 models. *Geophysical Research Letters*, *47*(17), e2020GL089964. doi: 10.1029/2020GL089964

Pidhorodetska, D., Fauchez, T. J., Villanueva, G. L., Domagal-Goldman, S. D., & Kopparapu, R. K. (2020). Detectability of molecular signatures on TRAPPIST-1e through transmission spectroscopy simulated for future space-based observatories. *The Astrophysical Journal Letters*, *898*(2), L33. doi:

10.3847/2041-8213/aba4a1

Pierrehumbert, R. T., & Hammond, M. (2019). Atmospheric circulation of tide-locked exoplanets. *Annual Review of Fluid Mechanics*, *51*, 275–303. doi: 10.1146/annurev-fluid-010518-040516

Pokrovsky, O. S., & Schott, J. (1999). Processes at the magnesium-bearing carbonates/solution interface. II. Kinetics and mechanism of magnesite dissolution. *Geochimica et Cosmochimica Acta*, *63*(6), 881–897. doi: 10.1016/S0016-7037(99)00013-7

Pope, E. C., Bird, D. K., & Rosing, M. T. (2012). Isotope composition and volume of Earth's early oceans. *Proceedings of the National Academy of Sciences*, *109*(12), 4371–4376. doi: 10.1073/pnas.1115705109

Press, W. H., Teukolsky, S. A., Vetterling, W. T., & Flannery, B. P. (1992). *Numerical Recipes in C, 2nd edition.* Cambridge University, New York.

Rasilo, T., Hutchins, R. H. S., Ruiz-González, C., & Del Giorgio, P. A. (2017). Transport and transformation of soil-derived CO_2, CH_4 and DOC sustain CO_2 supersaturation in small boreal streams. *Science of the Total Environment*, *579*, 902–912. doi: 10.1016/j.scitotenv.2016.10.187

Reid, W. H., & Harris, D. L. (1958). Some further results on the Bénard problem. *The Physics of Fluids*, *1*(2), 102–110. doi: 10.1063/1.1705871

Ringwood, A. E. (1991). Phase transformations and their bearing on the constitution and dynamics of the mantle. *Geochimica et Cosmochimica Acta*, *55*(8), 2083–2110. doi: 10.1016/0016-7037(91)90090-R

Rudnick, R. L., & Gao, S. (2003). Composition of the continental crust. In *Treatise on Geochemistry* (Vol. 3, p. 659). Elsevier.

Rushby, A. J., Johnson, M., Mills, B. J., Watson, A. J., & Claire, M. W. (2018). Long-term planetary habitability and the carbonate-silicate cycle. *Astrobiology*, *18*(5), 469–480. doi: 10.1089/ast.2017.1693

Saito, G., Kazahaya, K., Shinohara, H., Stimac, J., & Kawanabe, Y. (2001). Variation of volatile concentration in a magma system of Satsuma-Iwojima volcano deduced from melt inclusion analyses. *Journal of Volcanology and Geothermal Research*, *108*(1-4), 11–31. doi: 10.1016/S0377-0273(00)00276-6

Saito, H., & Kuramoto, K. (2018). Formation of a hybrid-type proto-atmosphere on Mars accreting in the solar nebula. *Monthly Notices of the Royal Astronomical*

Society, *475*(1), 1274-1287. doi: 10.1093/mnras/stx3176

Sanloup, C., Jambon, A., & Gillet, P. (1999). A simple chondritic model of Mars. *Physics of the Earth and Planetary Interiors*, *112*(1-2), 43–54. doi: 10.1016/S0031-9201(98)00175-7

Sata, N., Hirose, K., Shen, G., Nakajima, Y., Ohishi, Y., & Hirao, N. (2010). Compression of FeSi, Fe3C, $Fe_{0.95}O$, and FeS under the core pressures and implication for light element in the Earth's core. *Journal of Geophysical Research: Solid Earth*, *115*(B9). doi: 10.1029/2009JB006975

Schaefer, L., & Fegley, B. (2017). Redox states of initial atmospheres outgassed on rocky planets and planetesimals. *The Astrophysical Journal*, *843*(2), 120. doi: 10.3847/1538-4357/aa784f

Schulze-Makuch, D., Méndez, A., Fairén, A. G., Von Paris, P., Turse, C., Boyer, G., ... Irwin, L. N. (2011). A two-tiered approach to assessing the habitability of exoplanets. *Astrobiology*, *11*(10), 1041–1052. doi: 10.1089/ast.2010.0592

Schwieterman, E. W., Kiang, N. Y., Parenteau, M. N., Harman, C. E., DasSarma, S., Fisher, T. M., ... Lyons, T. W. (2018). Exoplanet biosignatures: a review of remotely detectable signs of life. *Astrobiology*, *18*(6), 663–708. doi: 10.1089/ast.2017.1729

Seager, S., Kuchner, M., Hier-Majumder, C., & Militzer, B. (2007). Mass-radius relationships for solid exoplanets. *The Astrophysical Journal*, *669*(2), 1279. doi: 10.1086/521346

Shahar, A., Driscoll, P., Weinberger, A., & Cody, G. (2019). What makes a planet habitable? *Science*, *364*(6439), 434–435. doi: 10.1126/science.aaw4326

Sleep, N. H., & Zahnle, K. (2001). Carbon dioxide cycling and implications for climate on ancient Earth. *Journal of Geophysical Research: Planets*, *106*(E1), 1373–1399. doi: 10.1029/2000JE001247

Smith, P. M., & Asimow, P. D. (2005). Adiabat_1ph: A new public front-end to the MELTS, pMELTS, and pHMELTS models. *Geochemistry, Geophysics, Geosystems*, *6*(2). doi: 10.1029/2004GC000816

Solomatov, V. S. (1995). Scaling of temperature-and stress-dependent viscosity convection. *Physics of Fluids*, *7*(2), 266–274. doi: 10.1063/1.868624

Spiegel, D. S., Menou, K., & Scharf, C. A. (2009). Habitable climates: the influence of obliquity. *The Astrophysical Journal*, *691*(1), 596. doi: 10.1088/0004-637X/

691/1/596

Stamenković, V., Noack, L., Breuer, D., & Spohn, T. (2012). The influence of pressure-dependent viscosity on the thermal evolution of super-Earths. *The Astrophysical Journal*, *748*(1), 41. doi: 10.1088/0004-637X/748/1/41

Tao, C., Seyfried, W., Lowell, R., Liu, Y., Liang, J., Guo, Z., ... Li, W. (2020). Deep high-temperature hydrothermal circulation in a detachment faulting system on the ultra-slow spreading ridge. *Nature Communications*, *11*(1), 1–9. doi: 10.1038/s41467-020-15062-w

Taylor, G. J. (2013). The bulk composition of Mars. *Geochemistry*, *73*(4), 401–420. doi: 10.1016/j.chemer.2013.09.006

Thompson, M. A., Krissansen-Totton, J., Wogan, N., Telus, M., & Fortney, J. J. (2022). The case and context for atmospheric methane as an exoplanet biosignature. *Proceedings of the National Academy of Sciences*, *119*(14), e2117933119. doi: 10.1073/pnas.2117933119

Thompson, R. N., Riches, A. J. V., Antoshechkina, P. M., Pearson, D. G., Nowell, G. M., Ottley, C. J., ... Niku-Paavola, V. (2007). Origin of CFB magmatism: multi-tiered intracrustal picrite–rhyolite magmatic plumbing at Spitzkoppe, western Namibia, during early Cretaceous Etendeka magmatism. *Journal of Petrology*, *48*(6), 1119–1154. doi: 10.1093/petrology/egm012

Tosca, N. J., McLennan, S. M., Lindsley, D. H., & Schoonen, M. A. (2004). Acid-sulfate weathering of synthetic Martian basalt: The acid fog model revisited. *Journal of Geophysical Research: Planets*, *109*(E5). doi: 10.1029/2003JE002218

Trail, D., Watson, E. B., & Tailby, N. D. (2011). The oxidation state of Hadean magmas and implications for early Earth's atmosphere. *Nature*, *480*(7375), 79. doi: 10.1038/nature10655

Treiman, A. H., & Schwenzer, S. P. (2009). Basalt–atmosphere interaction on Venus: Preliminary results on weathering of minerals and bulk rock. In *Venus Geochemistry: Progress, Prospects, and New Missions* (p. abstract #2011).

Trenberth, K. E., Fasullo, J., & Smith, L. (2005). Trends and variability in column-integrated atmospheric water vapor. *Climate dynamics*, *24*(7), 741–758. doi: 10.1007/s00382-005-0017-4

Turcotte, D. L., & Schubert, G. (2002). *Geodynamics*. Cambridge University Press.

Tyburczy, J. A., Duffy, T. S., Ahrens, T. J., & Lange, M. A. (1991). Shock wave equation of state of serpentine to 150 GPa: Implications for the occurrence of water in the Earth's lower mantle. *Journal of Geophysical Research: Solid Earth*, *96*(B11), 18011–18027. doi: 10.1029/91JB01573

Tziperman, E., Abbot, D. S., Ashkenazy, Y., Gildor, H., Pollard, D., Schoof, C. G., & Schrag, D. P. (2012). Continental constriction and oceanic ice-cover thickness in a Snowball-Earth scenario. *Journal of Geophysical Research: Oceans*, *117*(C5). doi: 10.1029/2011JC007730

Unterborn, C. T., Byrne, P. K., Anbar, A. D., Arney, G. N., Brain, D., Desch, S. J., ... Way, M. J. (2021). Exogeoscience and its role in characterizing exoplanet habitability and the detectability of life. *Bulletin of the American Astronomical Society*. doi: 10.3847/25c2cfeb.5209dd13

Unterborn, C. T., Dismukes, E. E., & Panero, W. R. (2016). Scaling the Earth: a sensitivity analysis of terrestrial exoplanetary interior models. *The Astrophysical Journal*, *819*(1), 32. doi: 10.3847/0004-637X/819/1/32

Unterborn, C. T., Foley, B. J., Desch, S. J., Young, P. A., Vance, G., Chiffelle, L., & Kane, S. R. (2022). Mantle degassing lifetimes through galactic time and the maximum age stagnant-lid rocky exoplanets can support temperate climates. *The Astrophysical Journal Letters*, *930*(1), L6. doi: 10.3847/2041-8213/ac6596

Unterborn, C. T., Kabbes, J. E., Pigott, J. S., Reaman, D. M., & Panero, W. R. (2014). The role of carbon in extrasolar planetary geodynamics and habitability. *The Astrophysical Journal*, *793*(2), 124. doi: 10.1088/0004-637X/793/2/124

Urey, H. C. (1952). *The Planets: their Origin and Development*. Yale Univ. Press.

Vance, S., Harnmeijer, J., Kimura, J., Hussmann, H., DeMartin, B., & Brown, J. M. (2007). Hydrothermal systems in small ocean planets. *Astrobiology*, *7*(6), 987–1005. doi: 10.1089/ast.2007.0075

Vervoort, P., Horner, J., Kane, S. R., Turner, S. K., & Gilmore, J. B. (2022). System architecture and planetary obliquity: Implications for long-term habitability. *The Astronomical Journal*, *164*(4), 130. doi: 10.3847/1538-3881/ac87fd

Vidaurri, M. R., Bastelberger, S. T., Wolf, E. T., Domagal-Goldman, S., & Koppapurapu, R. K. (2022). The outer edge of the Venus zone around main-sequence

stars. *The Planetary Science Journal*, *3*(6), 137. doi: 10.3847/PSJ/ac68e2

Wade, J. A., Plank, T., Melson, W. G., Soto, G. J., & Hauri, E. H. (2006). The volatile content of magmas from Arenal volcano, Costa Rica. *Journal of Volcanology and Geothermal Research*, *157*(1-3), 94–120. doi: 10.1016/j.jvolgeores.2006.03.045

Walsh, K. J., & Levison, H. F. (2019). Planetesimals to terrestrial planets: collisional evolution amidst a dissipating gas disk. *Icarus*, *329*, 88–100. doi: 10.1016/j.icarus.2019.03.031

Weider, S. Z. (2019). Petrology and geochemistry of Mercury. *Oxford Research Encyclopedia of Planetary Science*, 127. doi: 10.1093/acrefore/9780190647926.013.127

Weidner, D. J., Bass, J. D., Ringwood, A. E., & Sinclair, W. (1982). The single-crystal elastic moduli of stishovite. *Journal of Geophysical Research: Solid Earth*, *87*(B6), 4740–4746. doi: 10.1029/JB087iB06p04740

Wett, J. P., & Ahrens, T. J. (1983). Shock compression of single-crystal forsterite. *Journal of Geophysical Research: Solid Earth*, *88*(B11), 9500–9512. doi: 10.1029/JB088iB11p09500

Wordsworth, R. D., Forget, F., Selsis, F., Millour, E., Charnay, B., & Madeleine, J.-B. (2011). Gliese 581d is the first discovered terrestrial-mass exoplanet in the habitable zone. *The Astrophysical Journal Letters*, *733*(2), L48. doi: 10.1088/2041-8205/733/2/L48

Young, P. A., Desch, S. J., Anbar, A. D., Barnes, R., Hinkel, N. R., Kopparapu, R., ... Truitt, A. (2014). Astrobiological stoichiometry. *Astrobiology*, *14*(7), 603–626. doi: 10.1089/ast.2014.1143

Zhang, Y., & Zindler, A. (1993). Distribution and evolution of carbon and nitrogen in Earth. *Earth and Planetary Science Letters*, *117*(3-4), 331–345. doi: 10.1016/0012-821X(93)90088-Q

Table 5. Starting crustal compositions in mol% for continental weathering simulations. Horizontal lines delineate broad mineral groups: pyroxenes and olivines, feldspars, cyclosilicates, silica polymorphs, hornblende, secondary minerals, carbonates, sulfates, sulfides, and halides. Notes and references: [a] Sedimentary. [b] Hydrothermal. [c] Matches both oxide mass fractions from Rudnick and Gao (2003) and mineral volume fractions from Nesbitt and Markovics (1997) within 10% prior to the addition of carbonates, sulfates, sulfides, and halite. The kinetic parameters of annite and daphnite are assumed to be the same as those of phlogopite and clinochlore, respectively, from Palandri and Kharaka (2004). [d] Matches primitive mantle oxide mass fractions of Hofmann (1988) within 4% prior to addition of pyrite and halite. [e] From Table 3 (average Mercury Southern hemisphere composition) of Weider (2019), matching both mineral and elemental mass fractions, and attributing all hypersthene, olivine, and sulfide respectively as enstatite, forsterite, and pyrite to match the high Mg/Fe and S/Fe ratios. [f] Results of modeled interaction between basalt and Venus' atmosphere (Treiman & Schwenzer, 2009; Dyar et al., 2021). [g] Highland composition (Table 5.1 of Papike et al. (1998)) with feldspar composition from their Table A5.6, olivine composition from the Fe/(Fe+Mg) ratios of their Table A5.9, and Ca- and Mg-rich pyroxene compositions (attributed to 50% diopside / 25% enstatite / 25% wollastonite in case 1; 100% diopside in case 2) from columns 17 and 19 of their Table A5.4 due to the lack of kinetic data for Fe-pyroxene (ferrosilite) in Palandri and Kharaka (2004). [h] From the Martian upper crust experimental mineralogy used by Tosca et al. (2004) as reported in Table 24.3 of McLennan and Grotzinger (2008), with plagioclase attributed to albite based on the lack of anorthite in a Meridiani Planum outcrop (Table 23.3 of Ming et al. (2008)), oxides attributed to hematite, and addition of jarosite and anhydrite at abundances bracketed by the lack of sulfates in the Tosca et al. (2004) composition and the tens of mass% of sulfates in Table 24.3 of McLennan and Grotzinger (2008) and Table 26.2 of Des Marais et al. (2007). [i] Compositions for Fig. 4b and 5d of De Sanctis et al. (2015), assuming their optically dark component is magnetite.

Mineral	Formula	Earth[c] (modern)	Earth[d] (Archean)	Mercury[e]	Venus 1[f] (reduced)	Venus 2[f] (oxidized)	Lunar 1[g]	Lunar 2[g]	Mars[h]	Ceres 1[i]	Ceres 2[i]
Fayalite	Fe_2SiO_4	-	7.5	-	-	-	2.0	2.4	2.0	-	-
Forsterite	Mg_2SiO_4	-	53.6	8.5	-	-	4.9	5.3	10.7	-	-
Enstatite	$MgSiO_3$	-	27.2	51.1	38.8	12.2	9.5	-	23.8	-	-
Wollastonite	$CaSiO_3$	-	3.1	-	-	-	9.5	-	-	-	-
Diopside	$CaMg(SiO_3)_2$	-	-	4.3	-	-	18.9	32.4	-	-	-
Anorthite	$CaAl_2Si_2O_8$	8.4	4.7	11.7	-	-	16.5	17.7	-	-	-
Albite	$NaAlSi_3O_8$	15.6	1.5	17.9	11.8	11.2	0.9	0.9	12.3	-	-
K-feldspar	$KAlSi_3O_8$	5.0	-	0.4	-	-	0.1	0.2	0.4	-	-
Cordierite	$Mg_2Al_4Si_5O_{18}$	-	-	-	7.6	7.2	-	-	-	-	-
Quartz	SiO_2	59.7	-	-	12.2	31.1	-	-	-	-	-
Amorph. SiO_2	SiO_2	-	-	-	-	-	37.8	41.2	39.2	-	-
Anthophyllite	$Mg_7Si_8O_{22}(OH)_2$	0.21	-	-	-	-	-	-	-	-	-
Tremolite	$Ca_2Mg_5Si_8O_{22}(OH)_2$	0.43	-	-	-	-	-	-	-	-	-
Annite	$KAlFe_3Si_3O_{10}(OH)_2$	1.0	-	-	-	-	-	-	-	1.6	2.2
Phlogopite	$KAlMg_3Si_3O_{10}(OH)_2$	1.8	-	-	-	-	-	-	-	-	-
Daphnite	$Fe_5AlAlSi_3O_{10}(OH)_8$	1.4	-	-	-	-	-	-	-	-	-
Lizardite	$Mg_3Si_2O_5(OH)_4$	-	-	-	-	-	-	-	-	3.6	4.4
Magnetite	Fe_3O_4	-	-	-	-	-	-	-	-	57.1	72.3
Hematite	Fe_2O_3	-	-	-	-	9.9	-	-	7.1	-	-
Calcite	$CaCO_3$	4.8	-	–61–	-	-	-	-	-	-	-
Dolomite[a]	$CaMg(CO_3)_2$	1.7	-		-	-	-	-	-	-	
Dolomite[b]	$CaMg(CO_3)_2$	-	-		-	-	-	-	-	-	21.2
Magnesite	$MgCO_3$	-	-		-	-	-	-	-	37.7	-
Gypsum	$CaSO_4{\cdot}2H_2O$	0.89	-	-	-	-	-	-	-	-	-
Anhydrite	$CaSO_4$	-	-	-	29.6	28.4	-	-	2.8	-	-
Jarosite	$KFe_3(SO_4)_2(OH)_6$	-	-	-	-	-	-	-	1.8	-	-
Pyrite	FeS_2	0.17	0.21	6.1	-	-	-	-	-	-	-
Halite	NaCl	3.8	2.3	-	-	-	-	-	-	-	-